Climate Data Record (CDR) Program

Climate Algorithm Theoretical Basis Document (C-ATBD)

Remote Sensing Systems Version-7 Special Sensor Microwave/Imager Fundamental Climate Data Record

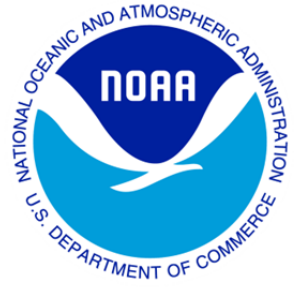

CDR Program Document Number: CDRP-ATBD-0100
Revision 2.0 March 28, 2013
CI#01B05

Copyright Statement

Acknowledgements:

The algorithms and computer code described by this documents were developed over the past decade with support from NASA Earth Sciences Program. Conversion of the brightness temperature dataset from a proprietary binary format to netcdf 4.0 format with CF 1.6 compliant metadata was performed with support from the NOAA Climate Data Record Program.

RESPONSIBILITY

Prepared By:	Hilawe Semunegus	Physical Scientist	NOAA/NCDC
	Signature		Date
Edited By:	Brian Newport	Lead Software Engineer	CDR Program
	Signature		Date
Reviewed By:	<Name>	<Title>	<Organization>
	Signature		Date
Approved By:	<Name>	<Title>	<Organization>
	Signature		Date
Approved By:	<Name>	<Title>	<Organization>
	Signature		Date

REVISION HISTORY

Version	Description	Revised Sections	Date
1.0	Initial submission to CDR Program	New Document	06/14/2011
2.0	Revised submission to reflect changes to processing for Version 7. Ref CR-0009. DSR-388.	Section 3 entirely rewritten. Minor edits were performed to reflect the version number change elsewhere in the document.	3/28/2013

TABLE of CONTENTS

LIST of FIGURES

LIST of TABLES

ACRONYMS AND ABBREVIATIONS

Acronym or Abbreviation	Meaning
AMSU	Advanced Microwave Sounding Unit
CATBD	Climate Algorithm Theoretical Basis Document
CDR	Climate Data Record
DMSP	Defense Meteorological Satellite Program
EUMETSAT	European Organisation for the Exploitation of Meteorological Satellites
FCDR	Fundamental Climate Data Record
GMAO	Global Modeling and Assimilation Office
GPCP	Global Precipitation Climatology Project
MEaSUREs	Making Earth Science Data Records for Use in Research Environments
MSU	Microwave Sounding Unit
NASA	National Aeronautics and Space Administration
NCDC	National Climatic Data Center
netCDF-4	network Common Data Form, Version 4.x
NOAA	National Oceanic and Atmospheric Administration
NSIDC	National Snow and Ice Data Center
RADCAL	Radar Calibration
REASoN	Research, Education and Applications Solution Network
RSS	Remote Sensing Systems
SBIR	Small Business Innovation Research
SSM/I	Special Sensor Microwave/Imager
T_A	Antenna temperature
T_B	Brightness temperature

1. Introduction

1.1 Purpose

The purpose of this document is to describe the algorithm submitted to the National Climatic Data Center (NCDC) by Hilawe Semunegus (NCDC) that will be used to create the RSS Version-7 SSM/I Fundamental Climate Data Record (FCDR), using the DMSP SSM/I series of instruments. The actual algorithm is defined by the computer program (code), and thus the intent here is to provide a guide to understanding that algorithm, from both a scientific perspective and in order to assist a software engineer performing an evaluation of the code.

1.2 Definitions

Following is a summary of the symbols used to define the algorithm.

Γ = Antenna Function

Ψ = Simplified RTM

T_s = Sea Surface Temperature

W = Surface Wind Speed

ϕ_w = Wind Direction

V = Total Column Water Vapor

L = Total Column Liquid Water

T_A = Antenna Temperature

T_B = Briightness Temperature

η = spillover

χ = cross-polarization coupling

β = sun zenith angle

α = sun azimuth angle

Λ = non-linearity function

θ_i = earth incidence angle

ϕ_r = relative angle between the wind direction and the SSM/I azimuth look direction

$\psi(\omega)$ = scan angle correction factor

ξ = target factor

φ = position of the satellite in its orbit

1.3 Products Generated

The Special Sensor Microwave Imagers (SSM/I) are a series of six satellite radiometers that have been in operation since 1987 under the Defense Meteorological Satellite Program (DMSP). These satellite sensors measure the natural microwave emission coming from the Earth's surface in the spectral band from 19 to 85 GHz. These emission measurements contain valuable information on many important climate variables including winds over the ocean, moisture and rain in the atmosphere, sea ice, and snow cover. However, the extraction of this information from the raw satellite measurements is a complicated process requiring considerable care and diligence. The first step in the process is the generation of Fundamental Climate Data Records (FCDR) of the sensor measurements in term of antenna temperatures (T_A) and brightness temperatures (T_B). It is absolutely essential that proper satellite inter-calibration methods be employed when producing these SSM/I FCDRs.

1.4 Instrument Characteristics

The radiometric characteristics of the seven SSM/I channels are listed in Table 1. These channels were selected to achieve specific objectives for measuring parameters. For example, a channel with a center frequency of 22.235 GHz was included in order to obtain estimates of atmospheric water vapor. The 19 and 37 GHz channels were used to achieve the maximum transfer of scientific experience and algorithms from the ESMR and SMMR instruments. The 85.5 GHz channels were chosen in order to more effectively measure rain and cloud properties. The channel bandwidths were chosen as a compromise between spectral sensitivity (requiring the narrowest spectral intervals) and sensor noise. For broadband signals, the measurement uncertainty due to noise is inversely proportional to the square root of the bandwidth, so larger bandwidths generally result in more accurate measurements. (Raytheon, 2000)

CHANNEL ABBREVIATION	CENTER FREQUENCY (GHz)	CENTER WAVELENGTH (cm)	BANDWIDTH (MHz)	POLARIZATION	INTEGRATION TIME (ms)
19V	19.35	1.549	240	Vertical	7.95
19H	19.35	1.549	240	Horizontal	7.95
22V	22.235	1.348	240	Vertical	7.95
37V	37.0	0.810	900	Vertical	7.95
37H	37.0	0.810	900	Horizontal	7.95
85V	85.5	0.351	1400	Vertical	3.89
85H	85.5	0.351	1400	Horizontal	3.89

Table 1: SSM/I Channel characteristics (Raytheon, 2000).

2. Algorithm Description

2.1 Algorithm Overview

The RSS Version-7 SSM/I FCDR dataset has incorporated geolocation corrections, sensor calibration (including cross-scan biases), and quality control procedures in a consistent way for the entire 16-year SSM/I dataset. In addition, brightness temperatures from the six SSM/Is (F08, F10, F11, F13, F14, and F15) have been intercalibrated which allows user to use these SSM/I products for detailed interannual and decadal trend studies.

2.2 Processing Outline

The processing outline for the RSS Version-7 SSM/I FCDR is summarized in Figure 1, which includes the basic elements such as input, output, and intercalibration as well as the conversion of the data to netCDF-4. The algorithm to create the RSS Version-7 SSM/I FCDR product is written in IDL 8.2. Input data is intercalibrated RSS T_A data in binary format and the output product is written in netCDF-4 format.

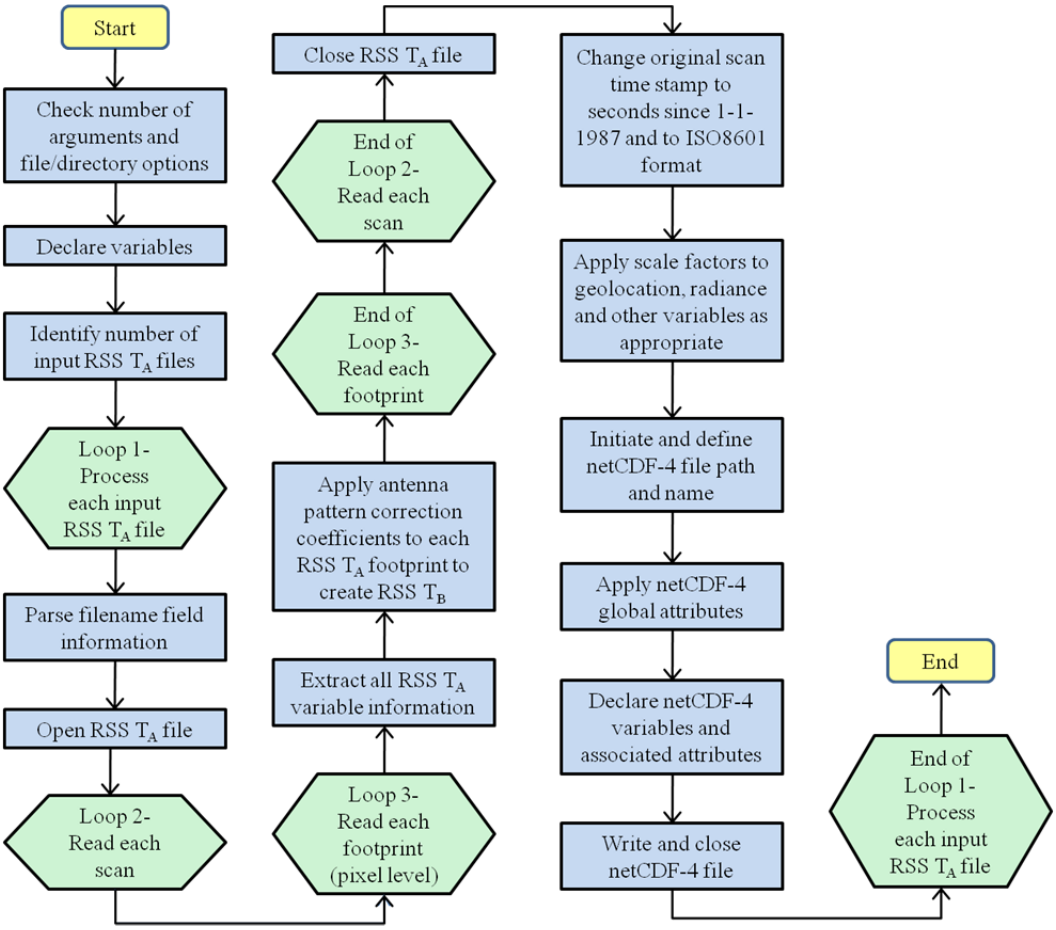

Figure 1: Flow chart for the creation of RSS Version-7 SSM/I FCDR

2.3 Algorithm Input

2.3.1 Primary Sensor Data

Original SSM/I antenna temperature data is generated after four processes: raw data acquisition, raw data unpacking, Earth location and tagging, and on-board calibration. Data is stored at RSS in a flat binary format, with one file for each SSM/I orbit. These files are the input data for the TA to TB algorithm described below.

2.4 Theoretical Description

2.4.1 Basic Formulation

The output of a microwave (MW) radiometer is a voltage that is converted to integer counts for the telemetry downlink. The first step of the calibration process is to convert these voltage counts to an antenna temperature T_A, which is discussed in Section 3.4.3. By definition, T_A is a measure of radiant power entering the feedhorn. It is the brightness temperature (T_B) of the surrounding environment integrated over the gain pattern of the SSM/I parabolic reflector and feedhorn assembly. In orbit, about ¾ of the surrounding environment consists of cold space at a temperature near 2.7 K, and the remaining ¼ is the Earth, which has a brightness temperature T_B between 100 and 300 K, depending on the scene. Thus, the antenna temperature is biased low relative to the Earth T_B, and this is called the spillover effect. In addition, some Earth scenes are very polarized, particularly the oceans, and the antenna gain pattern tends to mix polarizations. As a result, the antenna temperature is not as polarized as the Earth T_B, and this is called the cross polarization coupling effect. Section 3.4.4 expresses the relationship between T_A and T_B as

$$\mathbf{T_A} = \Gamma(\mathbf{T_B}) \qquad (1)$$

where $\mathbf{T_B}$ and $\mathbf{T_A}$ are the brightness temperatures and antenna temperatures for the 7 SSM/I channels. Herein, we use **boldface** to denote the array containing the full channel set of values. When expressed in non-boldface, it is the same quantity but for a single channel. The antenna function Γ depends on the antenna spillover η and cross polarization coupling χ, as definded in Section 3.4.4. The inverse of this relationship is called the antenna pattern correction (APC) and provides the means to retrieve brightness temperature values from the T_A measurements:

$$\mathbf{T_B} = \Gamma^{-1}(\mathbf{T_A}) \qquad (2)$$

The calibration process is done in terms of T_A rather than T_B because the former is the more fundamental measurement. A T_B value is a mixture of two SSM/I channels, and working in terms of T_B would make it more difficult to separate calibration problems

coming from different channels. There are other reasons for doing the calibration in terms of T_A which as discussed later.

The Version-7 calibration is heavily based on RSS most recent ocean radiative transfer model (RTM), which is also called V7. The basics of the ocean RTM are described by *Wentz* [1997] and *Wentz and Meissner* [2000]. More recent updates include *Meissner and Wentz* [2002, 2003, 2004, 2012]. The full RTM described [*Wentz and Meissner*, 2000] involves an radiative emissive and scattering rough ocean surface along with vertical integrations through the atmosphere. It has been shown that the full RTM is well represented by a simplified RTM, which herein we denote by the function Ψ:

$$\mathbf{T}_{\mathbf{B,rtm}} = \Psi\left(\mathbf{E}_{\mathbf{p}}\right) \tag{3}$$

$$\mathbf{T}_{\mathbf{A,rtm}} = \Gamma\left[\Psi\left(\mathbf{E}_{\mathbf{p}}\right)\right] \tag{4}$$

$$\mathbf{E}_{\mathbf{p}} = \left[T_s, W, \phi_w, V, L\right] \tag{5}$$

where $\mathbf{T_{B,rtm}}$ and $\mathbf{T_{A,rtm}}$ are the TOA T_B and T_A corresponding to the 7 channels. The set of environmental paramters ($\mathbf{E_p}$) includes sea-surface temperatue (T_s), sea-surface wind speed and direction (W, ϕ_w), columnar water vapor (V), and columnar liquid cloud water (L). Rain need not be considered because we exclude area of rain when doing the calibration. There are also secondary dependences such as the shape of the vapor and cloud vertical profiles in conjunction with the atmospheric temperature profile. The function $\Psi(\mathbf{E_p})$ is derived so that the effect of these secondary dependences when averaged globally over monthly time scale goes to zero. Implicit in (3) and (4) are the sensor parameters including the incidence and azimuth viewing angles θ_i and ϕ_i and the observation frequency.

In an important sense, the retrieval algorithm is the inverse of the RTM. For the retrieval algorithm, the inputs are either T_B or T_A measurements, and the output is the environmental parameters. We let Ψ^{-1} denote the retrieval algorithm while acknowledging that it is not a simple mathematical inverse of the RTM Ψ. For SSM/I, there is not enough orthogonal sensitivity in its 7 channels to retrieve T_s and ϕ_w, and these two parameters are treated as *a priori* arguments coming from NCEP fields. Thus the retrieval algorithm is denoted by

$$\mathbf{E}_{\mathbf{p}} = \Psi^{-1}\left[\mathbf{T}_{\mathbf{A}} \,|\, T_s, \phi_w; \eta, \chi\right] \tag{6}$$

where $\mathbf{T_A}$ denotes the input set of antenna temperatures for the different SSM/I channels. Formulating the retrieval algorithm in term of T_A rather than T_B requires that η and χ also be included as additional *a priori* arguments, and the retrieval algorithm is trained using simulated T_As rather than T_Bs. Our motivation for using a T_A-based retrieval algorithm is discussed in Section 3.4.4.

The degree to which the retrieval algorithm is a functional inverse of the RTM is determined by computing closure. This is done by inputting the three retrievals (*W*, *V*, *L*) into the RTM to predict the 7 SSM/I T_As. This closure calculation is represented by

$$\mathbf{T}_{\mathbf{A,rtm}} = \Gamma\left\{\Psi\left\{\Psi^{-1}\left[\mathbf{T}_{\mathbf{A}} \mid T_s, \phi_w; \eta, \chi\right]\right\}\right\} \tag{7}$$

and the degree of closure is measured by the difference between the RTM T_A minus the measurement T_A:

$$\boldsymbol{\delta}\mathbf{T}_{\mathbf{A,closure}} = \mathbf{T}_{\mathbf{A}} - \mathbf{T}_{\mathbf{A,rtm}} \tag{8}$$

There is no guarantee that one can precisely recover the 7 T_As given just 3 retrievals. Deficiencies in the RTM and/or retrieval algorithm along with calibration errors in the T_As will all degrade the closure. We will show that at this point in our development cycle the deficiencies in the RTM and retrieval algorithm are quite small, and $\boldsymbol{\delta T_{A,closure}}$ is mostly an indicator of calibration errors remaining in the T_A measurements. When calibration errors are removed, $\boldsymbol{\delta T_{A,closure}}$ is typical 0.1-0.2 K or less when averaged regionally over weekly time scales (see Figure 6 below). This high precision in closure allows us to achieve absolute calibration and inter-satellite calibration both in terms of $\mathbf{T_A}$ and $\mathbf{E_p}$ simultaneously.

Much of the calibration work is based on comparisons between the T_A measurements and $\mathbf{T_{A,rtm}}$. In addition, we use direct comparisons of T_A measurements. When directly comparing T_A measurements, it is necessary to normalize the measurements to a common incidence angle and antenna function Γ (i.e., common η and χ). In addition, since the azimuth viewing angles ϕ_i may be different for the two observations, the effect of wind direction on the observations needs to be removed. This normalization is done by first converting the T_A measurement to a brightness temperature using (2). The brightness temperature is then normalized as follows:

$$\mathbf{T}'_{\mathbf{B}} = \mathbf{T}_{\mathbf{B}} - \Psi\left(T_s, W, \phi_w, V, L; \theta_i\right) + \Psi\left(T_s, W, \cdots, V, L; \theta_{io}\right) \tag{9}$$

where the prime sign denotes normalization, θ_i is the actual incidence angle of the observation, and θ_{io}=53.25° is the common incidence angle to which all SSM/I observations are normalized. The time series plot of θ_i in the Appendix show that θ_i is usually within ±0.5° of θ_{io}. The second Ψ function in (9) is called the isotropic RTM for which the wind direction dependence is set to zero. The normalized brightness temperature is then converted back to an antenna temperature. For this conversion back to T_A, a common spillover η and cross-pol coupling χ are used for all 6 SSM/Is. We use the F13 η, χ values. The normalized T_A is then given by

$$\mathbf{T}'_{\mathbf{A}} = \Gamma_{F13}\left(\mathbf{T}'_{\mathbf{B}}\right) \tag{10}$$

2.4.2 Overview of Calibration Procedure

The first step in the calibration is to determine the antenna spillover η and cross polarization coupling χ, thereby establishing the absolute calibration of the SSM/I brightness temperatures. A prerequisite is to require that the $\mathbf{E_p}$ retrievals agree with *in situ* observation in an unbiased sense. The absolute calibration of wind speed is determined from anemometers on moored buoys that are part of the NDBC, TAO, TRITON, and PIRATA arrays. Water vapor absolute calibration is based on radiosonde and GPS measurements. For liquid cloud water, there are no *in situ* measurements extensive and accurate enough to meet our requirements. In this case, we use a statistical histogram method based on the fact that a significant portion of the SSM/I measurements will be free of clouds. This fact established a well determined zero-point for a histogram of cloud water. See *Wentz* [1997] for details. The absolute calibration criterion then requires that the mission-averaged T_A equals the RTM T_A

$$\left\langle \mathbf{T}_\mathbf{A} \right\rangle = \left\langle \mathbf{T}_{\mathbf{A,rtm}} \right\rangle \equiv \left\langle \Gamma\left[\Psi\left(\mathbf{E}_\mathbf{p} \right) \right] \right\rangle \tag{11}$$

where the brackets denote an average over the entire mission of a specified SSM/I. The antenna parameters η and χ, which are the implicit arguments of Γ, are then adjusted to satisfy the equality, as is described in Section 3.4.4. Early on in the calibration process, $\mathbf{E_p}$ comes from earlier versions of SSM/I processing and from other collocated satellites like WindSat. As the calibration process converges, $\mathbf{E_p}$ is the retrievals from the particular SSM/I being calibrated. Hence, a second SSM/I is not required by (11). The only requirement is that $\mathbf{E_p}$ is unbiased relative to the *in situ* observations. A final, small adjustment to η and χ is done at the end of the calibration procedure to ensure precise inter-satellite agreement of the geophysical retrievals, as is discussed later in this section.

The second step in the calibration is to find the relative calibration errors $\mathbf{\Delta T_A}$ for the 7 channels. These errors are subtracted from $\mathbf{T_{A0}}$, which is the T_A measurement derived from the radiometer counts given by (19) in Section 3.4.3, in order to obtained the 'true' antenna temperature $\mathbf{T_A}$:

$$\mathbf{T}_\mathbf{A} = \mathbf{T}_{\mathbf{A}0} - \mathbf{\Delta T}_\mathbf{A} \tag{12}$$

The relative errors depends on a number of parameters such as scan position, solar angles, position in orbit, etc., and these are listed later in this section. A given relative error is derived so that its mission average is near zero:

$$\left\langle \mathbf{\Delta T}_\mathbf{A} \right\rangle \approx 0 \tag{13}$$

In practice, the mission-average relative error will have a small bias depending on the details of how the mission-average is done, but in general the bias is less than 0.1 K, which is much smaller than the biasing due to the adjustments made to the antenna spillover and coupling. So the η, χ adjustment drives the absolute calibration.

The relative errors are found from inter-comparing observations from pairs of SSM/Is that were in operation at the same time. Table 2 gives the 11 pairs of overlapping SSM/Is. Two of these overlap are quite short: a few months or less. Two other overlaps include the end of the F10 mission during which there were problems. This leaves 7 overlaps that are considered primary and are used for calibration. Table 2 also shows the color coding that is used in Figure 17 below to display the 11 overlaps.

Table 2. The 11 Pairs of Inter-Satellite Overlaps and Their Color Coding for Figures

Primary	Short	Primary	Problem	Problem	Primary	Primary	Short	Primary	Primary	Primary
F08	F08	F10	F10	F10	F11	F11	F11	F13	F13	F14
F10	F11	F11	F13	F14	F13	F14	F15	F14	F15	F15
Black	Red	Green	Blue	Magenta	Cyan	Orange	Black	Red	Green	Blue

Two types of T_A inter-comparisons are done as represented by the following equations.

$$\delta \mathbf{T}_\mathbf{A}(i,j) = \mathbf{T}_\mathbf{A}(i) - \mathbf{T}_{\mathbf{A,rtm}}(j) \tag{14}$$

$$\delta \mathbf{T}'_\mathbf{A}(i,j) = \mathbf{T}'_\mathbf{A}(i) - \mathbf{T}'_\mathbf{A}(j) \tag{15}$$

where we have introduced the indices *i* and *j* as arguments to denote a pair of collocated SSM/Is. The first type of comparison (14) is between the T_A measurement of one SSM/I versus the RTM T_A predicted using the E_p retrievals from a second SSM/I. The second type of comparison (15) is the same as the first, except that the T_A measurements are first normalized to a common incidence angle and common η and χ. In addition, the normalization also removes the effect of wind direction. This normalization, which is denoted by the prime symbol, is accomplished by equations (9) and (10) and is intended to make the T_A measurements from two SSM/I directly comparable. For the first type of inter-comparison, the collocation criterion is based on daily, ¼° latitude/longitude maps. Separate maps are made for the ascending and descending orbit segments. The collocation criterion is that for a given map, a ¼° cell must contain observations from both SSM/Is. The collocation criterion is the same for the second type of inter-comparison except the maps are 5-day (pentad), 1° latitude/longitude maps.

We consider the most important scientific criterion for inter-satellite calibration is that the collocated geophysical retrievals from pairs of SSM/Is precisely agree. This is particularly important when constructing multi-decadal time series from the 25 years of SSM/I observations. Thus as the final step in the calibration procedure, we require the wind, vapor, and cloud retrievals from the pairs of SSM/I to precisely agree. In this case, the inter-satellite comparison is represented by

$$\delta \mathbf{E}_{\mathbf{p}}(i,j) = \mathbf{E}_{\mathbf{p}}(i) - \mathbf{E}_{\mathbf{p}}(j) \qquad (16)$$

The $\delta \mathbf{E}_{\mathbf{p}}(i, j)$ differences for the 7 primary overlaps are minimized by making small adjustments to the antenna parameters η and χ. Adjustments to η and χ produce changes in the retrievals as indicated by (6). While minimizing $\delta \mathbf{E}_{\mathbf{p}}(i, j)$, we continue to required that (11) is satisfied as closely as possible. Imposing these two constraints simultaneously (i.e., the minimization of $\delta \mathbf{E}_{\mathbf{p}}(i, j)$ and the T_A agreement with the RTM) provides the final values for η and χ. When averaged over the overlap periods, the procedure minimizes the inter-satellite wind and vapor differences to about 0.01 m/s and 0.01 mm. After accounting for diurnal variation, inter-satellite cloud differences are minimized to 0.0002 mm. In addition, the mission averaged T_A minus $T_{A,rtm}$ differences are typically 0.05 K.

There are 5 kinds of relative T_A adjustments:

$$\Delta \mathbf{T}_{\mathbf{A}} = \Delta \mathbf{T}_{\mathbf{A},\omega} + \Delta \mathbf{T}_{\mathbf{A},\mathbf{ht}} + \Delta \mathbf{T}_{\mathbf{A},\mathbf{isat}} + \Delta \mathbf{T}_{\mathbf{A},\mathbf{drift}} + \Delta \mathbf{T}_{\mathbf{A},\mathbf{tf}} \equiv \sum_{k=1}^{5} \Delta \mathbf{T}_{\mathbf{A},\mathbf{k}} \qquad (17)$$

where:

$\Delta \mathbf{T}_{\mathbf{A},\omega}$ is the along-scan adjustment (Section 3.4.5)

$\Delta \mathbf{T}_{\mathbf{A},\mathbf{ht}}$ is the adjustment to the hot target temperature (Section 3.4.6)

$\Delta \mathbf{T}_{\mathbf{A},\mathbf{isat}}$ is an adjustment that is unique and specific for the F08, F10, and F15 SSM/I (Sections 3.4.7, 3.4.8, and 3.4.9)

$\Delta \mathbf{T}_{\mathbf{A},\mathbf{drift}}$ is a small drift correction applied to F11 and F13 SSM/I (Section 3.4.10)

$\Delta \mathbf{T}_{\mathbf{A},\mathbf{tf}}$ is the 'target factor' adjustment (Section 3.4.11)

These adjustments are found so as to minimize either $\delta \mathbf{T}_{\mathbf{A}}(i, j)$ or $\delta \mathbf{T}'_{\mathbf{A}}(i, j)$ as is explained in the subsequent sections.

The adjustments are derived one at a time. Once a given adjustment is found, it is applied to the T_A measurement, and then the next adjustment is found. Once all adjustments are found, we repeat the procedure and find residual adjustments. The residual adjustments are very small (i.e., we get nearly the same adjustment the second time around). For example according to this procedure, when equation (14) to find the n^{th} adjustment $\Delta \mathbf{T}_{\mathbf{A},\mathbf{n}}$, the value of $\mathbf{T}_{\mathbf{A}}$ in (14) is

$$\mathbf{T}_{\mathbf{A}} = \mathbf{T}_{\mathbf{A}0} - \sum_{k \neq n} \Delta \mathbf{T}_{\mathbf{A},k} \qquad (18)$$

which says that all adjustments other than the adjustment currently being derived are applied to $\mathbf{T}_{\mathbf{A0}}$. The same holds true when equation (15) is being used to derive the adjustment.

Using inter-satellite comparisons to find the $\mathbf{\Delta T_A}$ risks the possibility of calibration errors from one sensor aliasing into another. We call this sensor error crosstalk. To assess this problem, we experimented with many variations of the calibration procedure presented here, such as using different pairs of SSM/Is to derive the same adjustments. For most types of errors, sensor error crosstalk does not appear to be a problem. As an example, when finding the along-scan adjustment $\mathbf{\Delta T_{A,\omega}}$, a given along-scan cell position for the first SSM/I will tend to randomly collocate with all the cell positions for the second SSM/I. As a result, the ω-errors in the first SSM/I do not alias into $\mathbf{\Delta T_{A,\omega}}$ for the second SSM/I. Furthermore, on the second iteration of the calibration procedure, the errors in the reference SSM/I are mostly removed. The one case where sensor error crosstalk is of concern is the F13 time drift, which is discussed in Section 3.4.10.

Another question on the robustness of the calibration procedure is the orthogonality of the 5 adjustments. Can a given calibration error be represented by more than one type of adjustment? The 5 types of adjustments have been designed to be dissimilar so as avoid this problem. Also, we have gone through many iterations of the calibration process, and the order of finding the 5 adjustments did not seem to really matter as long as two complete iterations of all 5 adjustments is done. Furthermore, any creeping of a calibration error from one type of adjustment to another has little effect on the overall calibration because the adjustments are added together. The only possible problem is the interpretation of the individual errors sources may be a bit skewed.

A useful calibration tool is the degree of closure as expressed by (8), or equivalently by (14) with $i = j$. It would be very convenient if $\mathbf{\delta T_{A,closure}}$ could be used to infer the T_A adjustments because one would then not need to rely on collocations with another SSM/I. However, if the $\mathbf{E_P}$ from the same satellite to compute $\mathbf{T_{A,rtm}}$, then the errors in $\mathbf{E_p}$ due to calibration errors $\mathbf{\Delta T_A}$ would be highly correlated with $\mathbf{\Delta T_A}$, and this correlation would tend to hide and/or distort the derivation of $\mathbf{\Delta T_A}$. This is why we use the $\mathbf{E_P}$ from a different SSM/I to compute $\mathbf{T_{A,rtm}}$. The E_p errors from a second SSM/I are much less correlated with the $\mathbf{\Delta T_A}$ errors of the first SSM/I. That is not to say $\mathbf{\delta T_{A,closure}}$ is not useful. In fact, it is an extremely useful tool for verification and diagnosing residual calibration error as is shown in Section 3.4.7 for the F08 SSM/I. The diagnostic $\mathbf{\delta T_{A,closure}}$ is best used as a final step after all known calibration errors are removed.

2.4.3 Unadjusted Antenna Temperature

In computing the unadjusted SSM/I antenna temperature, the basic assumption is that the radiometer output voltage expressed as counts is linearly related to the input power at the feedhorn expressed as T_A. Nonlinear effects such as imperfections in the square-law detector and the IF amplifier compression are assumed to negligible. Under these assumptions, antenna temperature is

$$T_{A0} = \frac{(T_h - T_c)C_e + T_c C_h - T_h C_c}{C_h - C_c} \qquad (19)$$

where the subscript *0* denotes no adjustments have been made. The terms C_c, C_h, and C_e are the radiometer counts when the radiometer is looking at the cold calibration target, the hot calibration target, and the earth scene, respectively. The temperatures T_c and T_h are the effective temperatures of the cold and hot calibration targets. Equation (19) is simply expressing the assumption that the radiometer counts vary linearly as the scene temperature varies from T_c to T_h.

The first difficulty in the calibration process is accurately specifying T_c and T_h. For example, the cold target is a mirror pointing towards cold space, which has a temperature of 2.73 K (i.e., the cosmic background temperature). However, if the mirror is not a perfect reflector or if the mirror is receiving some radiation from other sources such as the spacecraft or the Earth, the true value for T_c will be greater than 2.73 K. The specification of T_h is even more difficult. In this case, one must infer T_h from thermistor readings attached to the hot target. There will be some error in using these readings to estimate the effective emission temperature of the hot target. For example, thermal gradients, both horizontal and vertical, over the extent of the hot target will cause problems. SSM/I has only 3 thermistors attached to the hot target.

Our specification of the cold target temperature is

$$T_c = T_{c,plk} + \delta T_c \qquad (20)$$

The first term $T_{c,plk}$ is the Planck-adjusted value of cold space. The relationship between radiation intensity and temperature is given by Planck's law. In the lower microwave spectrum, this relationship is nearly linear and the Rayleigh-Jeans approximation is used. However as the frequency increases, the Rayleigh-Jeans approximation begins to break down. This effect can be compensated for by adjusting the cold space temperature. By doing this, one can continue to assume a linear relationship between radiation and temperature. This is standard practice and the value for $T_{c,plk}$ is 2.752, 2.761, 2.822, and 3.203 K for the four SSM/I frequencies (19, 22, 37, and 85 GHz). The second term δT_c is a small offset we apply to account for radiation coming from sources other than cold space such as the spacecraft and Earth. A value of δT_c = 0.3 K is used for all channels and all SSM/Is. This value assumes 0.2% of the radiation comes from the spacecraft and earth, which have a typical temperature of 150 K. We know the effective temperature of the cold target must be higher than cold space, and the inclusion of δT_c is a small hedge for this. We use this 0.3 K offset for all satellite MW imagers including AMSR-E, WindSat, TMI, and SSM/IS.

Our specification of the hot target temperature is

$$T_h = T_{h,therm} + \delta T_h \qquad (21)$$

The first term $T_{h,therm}$ is the hot target temperature derived just from the thermistors measurements, and the second term δT_h is a small offset we apply to account for an overall bias in the effective hot target temperature. A value of δT_h = −1.0 K is used for all channels and all SSM/Is. The inclusion of δT_h results in slightly better agreement

between the antenna spillover values derived herein and pre-launch values, as is discussed in Section 5. $T_{h,therm}$ is given by

$$T_{h,therm} = t_h + \xi\left(t_p - t_h\right) \tag{22}$$

The temperature t_h is the average of the 3 thermistor readings attached to the hot target and the temperature t_p is the reading from the single thermistor on the SSM/I drum plate facing the hot target. The coefficient ξ is a value derived from prelaunch thermal-vacuum measurements, and its value is 0.01 [*Hollinger et al.*, 1987]. Equation (22) is saying 99% of the hot target radiation is coming from the hot target itself and 1% of the radiation is coming from the reflection of the drum face off the hot target. For the F13 SSM/I, only hot-target thermistor 2 is used for t_h because the other 2 thermistors displayed considerable noise [*Colton and Poe*, 1999].

Noise in C_c and C_h is reduced by averaging measurements from adjacent scans. We use a time window of ±12 seconds centered on the scan being processed. If there are no data gaps, this time window will include 13 scans. For the 19-37 GHz channels, calibration counts are only collected every other scan. For 85 GHz, calibration counts are collected every scan. For each scan, 5 calibration measurements are taken of the cold target and another 5 for the hot target. Thus our ±12 seconds time window provides 35 cold counts and 35 hot counts for each of the lower-frequency channels and 65 counts at 85 GHz. This is a sufficient number of samples to reduce the noise in the calibration counts to an acceptable level.

2.4.4 Absolute Calibration

As previously discussed, the antenna temperature is a measure of radiant power entering the feedhorn. It is the brightness temperature of the surrounding environment integrated over the gain pattern of the SSM/I parabolic reflector and feedhorn assembly. This integration can be well approximated by [*Wentz*, 1991]

$$T_{Ai} = q_i T_{Bi} + \chi_i q_i T_{Bj} + \eta_i T_{c,plk} \tag{23}$$

$$q_i = \frac{1-\eta_i}{1+\chi_i} \tag{24}$$

where the spillover η is the fraction of received power coming from cold space and the cross polarization coupling χ is fractional power coming from the orthogonal polarization. The subscript i denotes polarization: $i = v$ or h, and the subscript j denotes the orthogonal polarization. When $i = v$, then $j = h$, and when $i = h$, then j = v. $T_{c,plk}$ is the Planck-adjusted value of cold space given in Section 3.4.3. The inverse of this relationship is called the antenna pattern correction (APC) and is given by

$$T_{Bi} = \frac{q_j T_{Ai} - \chi_i q_i T_{Aj} + \left(\chi_i q_i \eta_j - q_j \eta_i\right) T_{c,plk}}{q_i q_j \left(1 - \chi_i \chi_j\right)} \qquad (25)$$

In the more abbreviated notation used by equation (1) and (2), we let the antenna function $\Gamma(\mathbf{T_B})$ denote the conversion of T_B to T_A for all 7 SSM/I channels, and likewise $\Gamma^{-1}(\mathbf{T_A})$ is the APC function for all channels.

There is no 22 GHz h-pol T_A measurement for SSM/I, and hence (25) cannot be used to find the 22 GHz T_B. To avoid this problem, the input to the geophysical retrieval algorithm is T_A rather than T_B, and the calibration is also done in terms of T_A rather than T_B, as discussed in Section 3.4.1. This avoids having to convert the single-pol 22 GHz T_A into a T_B.

Absolute calibration of the SSM/I T_A measurements to the RTM as dictated by (11) can be obtained by varying η and χ so that the mission averaged T_A measurements agree with RTM. Since there are two unknowns (η and χ) for each channel, the estimation must be constrained in some way. We make the assumption that η and χ are the same for both polarizations:

$$\begin{aligned} \eta_v &= \eta_h \\ \chi_v &= \chi_h \end{aligned} \qquad (26)$$

For the dual polarization channels, the constraint imposed by (26) results in two unknowns for each polarization pair. The parameters η and χ are then varied to satisfy equation (11) for both polarizations.

At 22 GHz for which there is only the v-pol measurement, we need to employ an additional constraint to find both η and χ. The vapor retrievals for the F13 SSM/I are compared to collocated and validated WindSat vapor retrievals. The validation of the WindSat vapor retrievals is based on comparisons with GPS values, and these comparisons show good, unbiased agreement over the full range of water vapor from 0 to 65 mm. The vapor retrievals are driven by the 22-GHz measurements, and the 0 to 65 mm range corresponds to a range in the 22V T_A of about 75 K. This provides enough dynamic range to estimate both the offset and the slope of the SSM/I minus WindSat vapor difference. The parameters η and χ are found so as to make the SSM/I vapor retrievals agree with Windsat while satisfying equation (11). These two constraints then provide the means for finding both η and χ at 22 GHz. The value found for χ is 0.01560 as compared to the pre-launch value of 0.00983. This is a small change, equivalent to about 0.3 K in T_A. Rather than trying to do this type of analysis for each SSM/I, we simply use χ_{22v}=0.01560 for all SSM/Is. Having fixed χ_{22v}, then η_{22v} becomes the single parameter used to satisfy equation (11) for the other SSM/Is.

Assumption (26) that the spillover and polarization coupling is the same for both polarizations is supported by both pre-launch antenna pattern measurements and on-orbit SSM/I observations of heavily forested areas. *Hollinger et al.* [1987] report the same F08 SSM/I pre-launch spillover values for v-pol and h-pol. The reported polarization difference in χ ranged from 0.0006 to 0.005 (equivalent to about 0.05-0.25

K in T_A). Pre-launch antenna measurements of the other SSM/Is also indicate little polarization difference for η and χ [*Colton and Poe*, 1999].

The other evidence that supports (26) is the SSM/I observations of heavily forested areas where the v-pol and h-pol T_B are nearly the same. Setting $T_{Bv} = T_{Bh}$ in (23) gives

$$T_{Ai} = (1-\eta_i)T_B + \eta_i T_{c,plk} \qquad (27)$$

Analysis of the SSM/I T_A observations of these heavily forested areas shows little if any polarization difference. Hence according to (27), this implies $\eta_v = \eta_h$.

Tables 3 and 4 give the spillover and polarization coupling for the 6 SSM/Is respectively. These values are from the final step in the calibration process that minimizes both $\mathbf{\delta E_p}(i, j)$ and $T_A - T_{A,rtm}$, as discussed in Section 3.4.2. Figures 2 and 3 compare these spillover and polarization coupling values with those reported by *Colton and Poe* [1999], which are derived from pre-launch antenna range measurements. For spillover, typical differences between the values in Table 3 and the antenna range measurements are about 0.005. For an Earth scene of 200 K, this difference in η corresponds to 1 K. Spillover is a difficult parameter to infer from antenna range measurements, and an error of 0.005 is certainly reasonable.

For polarization coupling, there is a systematic bias between the values we infer and the values inferred from the antenna range measurements, with our values being higher. The exception is at 19 GHz, for which there is good agreement. This might suggest that the χ discrepancy, which is equivalent to about 0.5 K in T_B, may be due to a polarization problem with RTM. However, when this same type of analysis is applied to WindSat, AMSR-E, and SSM/IS, we find χ values in good agreement (0.2 K) with the ground-based measurement of χ. Thus for SSM/I, we attribute the χ discrepancy to the ground-based measurements somewhat underestimating the polarization coupling.

It should be noted that an error in η and an error in the hot target temperature T_h have nearly the same effect on the calculation of T_B. They both introduce a multiplicative bias in T_B. The 1 K reduction of the hot target temperature as given by the thermistors (see Section 4) results in our derived spillover values shown in Table 3 and Figure 2 being 0.004 higher. As Figure 2 shows, this increase in η results in slightly better agreement with the pre-launch values when considering all SSM/Is and all frequencies. We have observed the same phenomenon with AMSR-E, WindSat, and SSM/IS: decreasing the thermistor T_h by 1 K results in spillover values that better agree with pre-launch measurements. Whether this is real (i.e, the effective temperature of the hot target is indeed a little less than the thermistor value) is difficult to say for sure. In any event, for nearly all applications it does not matter whether you assign this small error to η or T_h.

For a given frequency, there is some variation of η and χ among the 6 SSM/Is. The pre-launch values and our values show about the same standard deviation among the 6 SSM/Is, except for the pre-launch spillover values for 22 GHz, which exhibit a relatively high standard deviation of 0.004. The standard deviation of our η and χ among the 6 SSM/I is about 0.0015 and 0.002, respectively. For an ocean scene of 225 K for v-pol

and 175 K for h-pol, the η variation of 0.0015 corresponds to about 0.3 K, and the χ variation of 0.002 corresponds to about 0.1 K. Although the pre-launch values and our values have about the same standard deviations among the sensors, the correlation between the two sets of values is small. All R^2 correlations are below 0.3, except for the 85 GHz χ values which have a correlation of 0.89. Thus, when it comes to inter-satellite calibration at the 0.1 K level, there is a significant difference between using the pre-launch η, χ values and the values derived herein.

Table 3. Spillover (η) for the 6 SSM/Is

	19 GHz	22 GHz	37 GHz	85 GHz
F08	0.02893	0.02504	0.02272	0.02014
F10	0.02586	0.02419	0.01804	0.01679
F11	0.02670	0.02315	0.01975	0.01360
F13	0.02618	0.02406	0.02007	0.01697
F14	0.02735	0.02528	0.01894	0.01678
F15	0.02688	0.02359	0.01918	0.01748

Table 4. Polarization Coupling (χ) for the 6 SSM/Is

	19 GHz	22 GHz	37 GHz	85 GHz
F08	0.00753	0.01560	0.03059	0.02650
F10	0.00665	0.01560	0.03376	0.03459
F11	0.00329	0.01560	0.03339	0.03194
F13	0.00518	0.01560	0.03283	0.02919
F14	0.00633	0.01560	0.03093	0.02962
F15	0.00777	0.01560	0.02882	0.03013

2.4.5 Along-Scan Correction

One of the first SSM/I calibration problems that was detected was an along-scan error [*Wentz*, 1991]. Towards the end of the Earth scan, the cold target mirror begins to intrude into the field of view of the feedhorn. As a result, the T_A measurements exhibit a systematic roll-off of about 1 K at the end of the scan. Our model for the along-scan error is to assume the radiation entering the feedhorn is a combination of Earth radiation $T_{A,earth}$ reflected off the parabolic antenna and cold space radiation $T_{c,plk}$ reflected off the cold target mirror:

$$T_{A0} = \left[1 - \mu(\omega)\right] T_{A,earth} + \mu(\omega) T_{c,plk} \qquad (28)$$

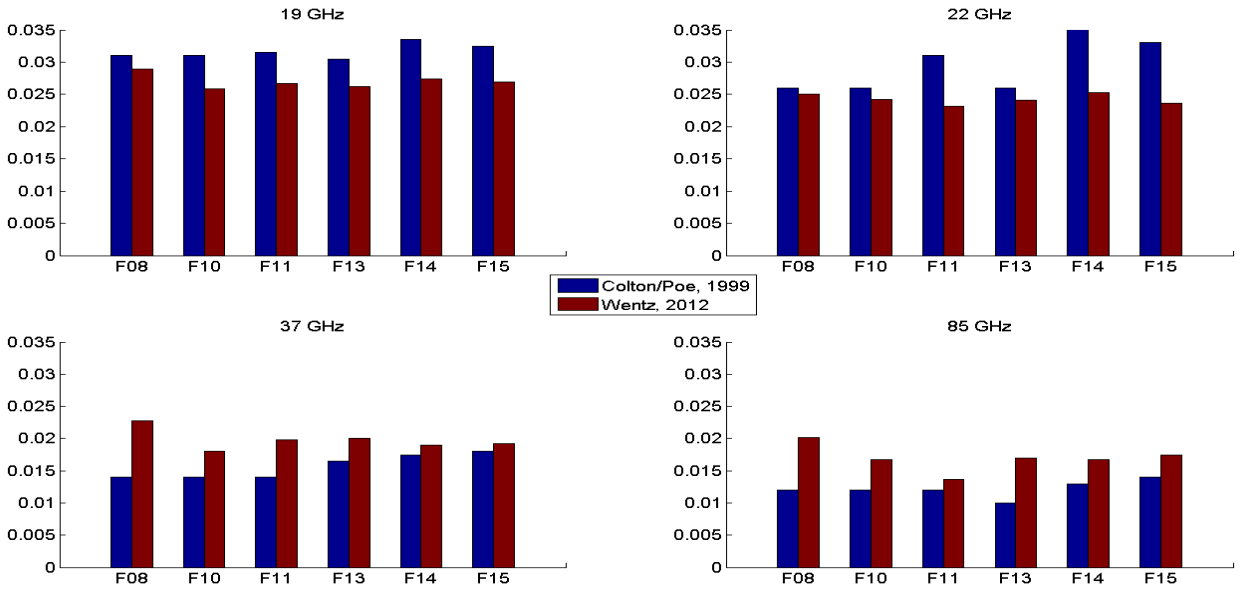

Figure 2. A comparison of the spillover η values obtained from pre-launch antenna range measurements [*Colton and Poe*, 1999] versus the values derived herein using the ocean RTM as the absolute calibration reference.

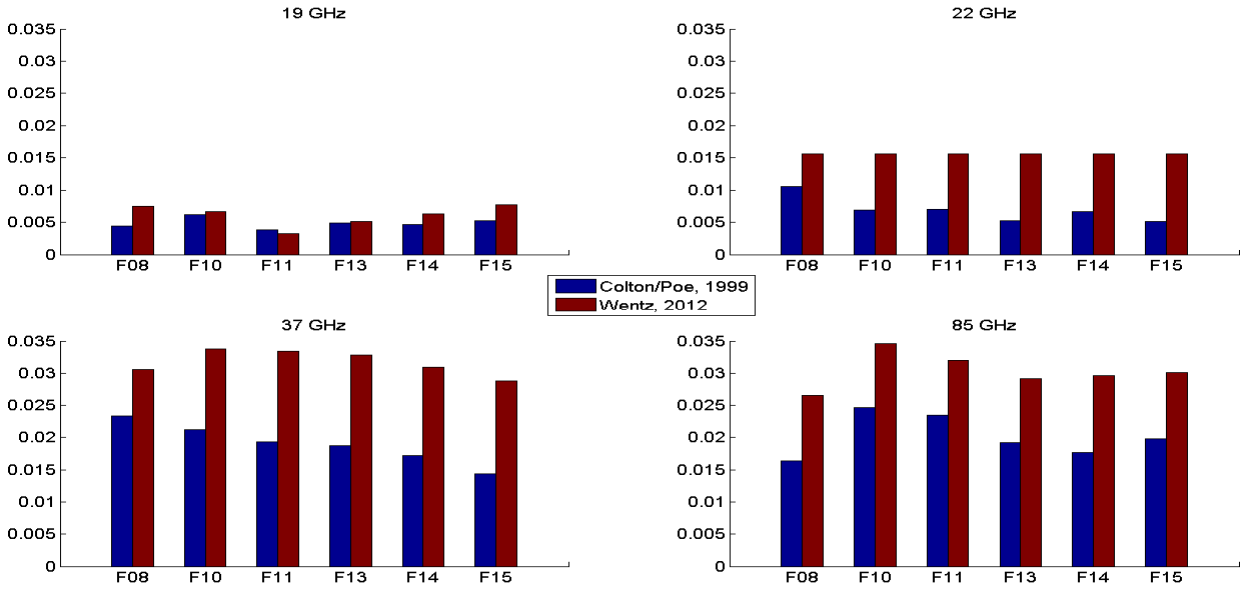

Figure 3. A comparison of the polarization coupling χ values obtained from pre-launch antenna range measurements [*Colton and Poe*, 1999] versus the values derived herein using the ocean RTM as the absolute calibration reference. The pre-launch values are systematically lower than those derived from the RTM. Other MW sensors like WindSat show better χ agreement with the RTM.

where μ(*ω*) is a function of the along-scan position *ω*. Since $T_{A,earth}$ is the desired quantity, the required adjustment according to (12) and (28) is

$$\Delta T_{A,\omega} = \frac{-\mu(\omega)}{1-\mu(\omega)}\left(T_{A0} - T_{c,plk}\right) \tag{29}$$

Of the five relative T_A adjustments, the derivation of along-scan correction $\Delta T_{A,\omega}$ is probably the most straightforward and provides a good example of how inter-satellite T_A differences are used for the derivation. In this case we use the inter-satellite T_A differences $\delta T_A(i, j)$ defined by (14). Table 5 lists the *i*, *j* sensor pairs use to determine μ(*ω*). $\delta T_A(i, j)$ represent millions of collocated sensor-*i* minus sensor-*j* T_A differences. As discussed in Section 3.4.2, when computing $\delta T_A(i, j)$ all adjustments are applied other than the $\Delta T_{A,\omega}$ currently under consideration. Thus the assumption can be made that $\delta T_A(i, j)$ equals $\Delta T_{A,\omega}$. This assumption becomes more rigorous as the calibration procedure iterates and the various adjustments converged. Assuming $\delta T_A(i, j) = \Delta T_{A,\omega}$ and inverting (29) to yield μ(*ω*) gives

$$\mu(\omega) = \frac{\delta T_A(i, j)}{\delta T_A(i, j) - \left(T_{A0} - T_{c,plk}\right)} \tag{30}$$

There are 64 scan positions for the 19-37 GHz channels and 128 positions for 85 GHz. Averages of μ(*ω*) are found for each scan position thereby creating μ(*ω*) tables. Figure 4 shows the μ(*ω*) tables for all satellites and all channels. The color coding used to display the 7 different channels is given in Table 6. Table 6 also gives the color coding for figures to be presented later in which the colors denote the 6 different SSM/Is. It should be noted that we also tried other pairs of sensors (i.e., different from Table 5) and got essential the same μ(*ω*).

Table 5. Pairs of Sensors Used to Determine Along-Scan Correction μ(*ω*)

SSM/I being calibrate: *i*	Sensor Used to Specify $\mathbf{E_P}$: *j*
F08	F10
F10	F11
F11	F13
F13	WindSat
F14	F13
F15	F13

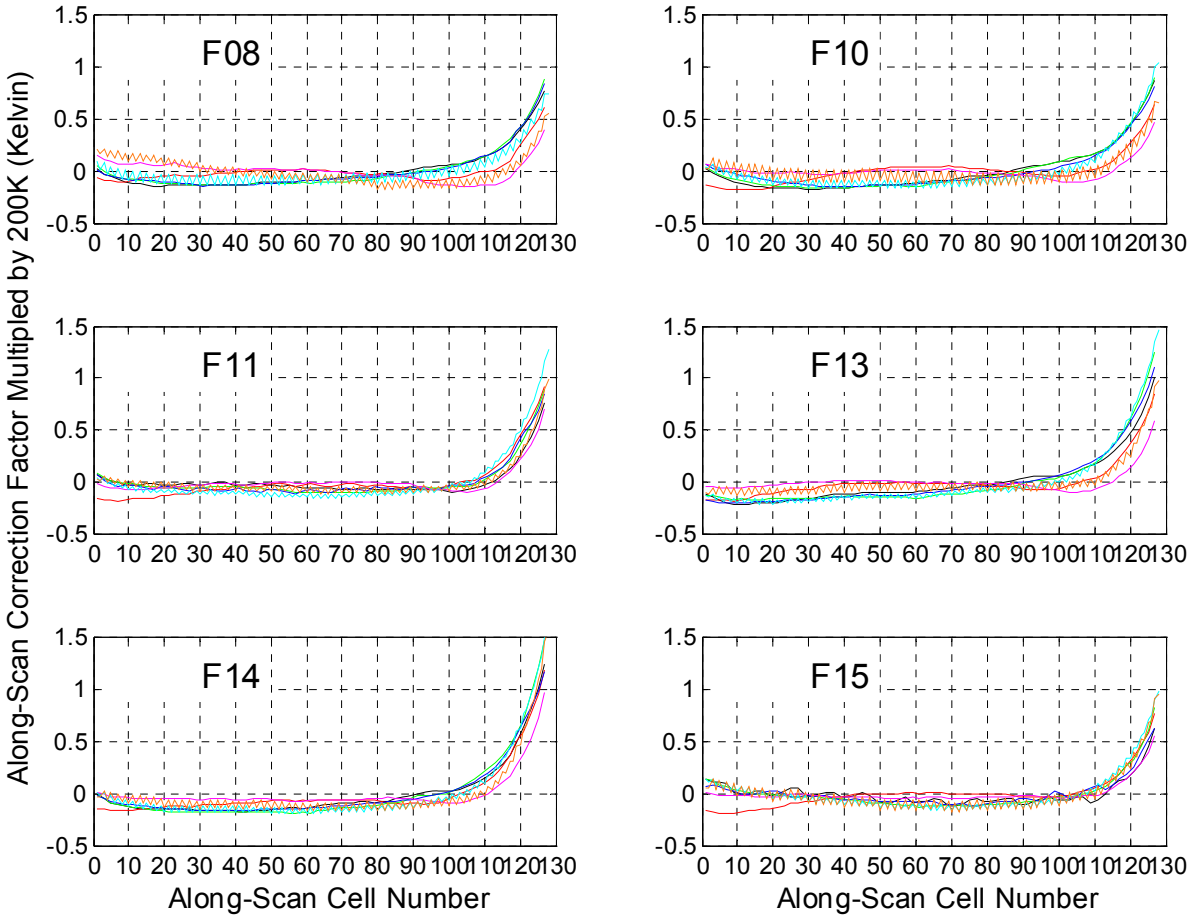

Figure 4. The along-scan correction that is applied to the SSM/I T_A. To show these results in terms of a value indicative of the T_A adjustment, $\mu(\omega)$ has been multiplied by 200 K. The adjustment has the effect of increasing T_A at the end of the scan to compensate for the intrusion of the cold mirror into the field of view. The 7 colors correspond to the 7 channels as indicated in Table 6. The 85 GHz channels show a 0.05 K saw-tooth pattern presumably due to a small mismatch in the integration timing.

Table 6. Color coding for figures displaying 7 channels or 6 SSM/Is.

	Black	Red	Green	Blue	Magenta	Cyan	Orange
Color Code for Channels	19V	19H	22V	37V	37H	85V	85H
Color Code for SSM/Is	F08	F10	F11	F13	F14	F15	

2.4.6 Adjustments to the Hot Target Temperature

As discussed in Section 3.4.3, the specification of the hot target temperature T_h is problematic. One must infer T_h from thermistor readings attached to the hot target. However, there will be some error in using these readings to estimate the effective emission temperature of the hot target. For example, the SSM/I has only 3 thermistors, and thermal gradients, both horizontal and vertical, over the extent of the hot target will introduce error. Such problems have been reported for both WindSat and the F16 SSM/IS [*Twarog et al*., 2006; *Sun and Weng*, 2008]. Herein, we find a similar problem for the SSM/Is.

The hot target temperature adjustment is found in a way analogous to that described in Section 3.4.5 for the along-scan correction. The change to T_A due to an error ΔT_h in specifying the hot target temperature is given by

$$\Delta T_{A,ht} = \frac{T_A - T_c}{T_h - T_c} \Delta T_h \qquad (31)$$

This is equivalent to adding ΔT_h to T_h in equation (19). Following the procedure described in Section 3.4.5, the assumption is made that $\delta T_A(i, j) = \Delta T_{A,ht}$ and (31) is inverted to yield ΔT_h.

$$\Delta T_h = \frac{T_h - T_c}{T_A - T_c} \delta T_A(i, j) \qquad (32)$$

To obtain a more robust estimate for ΔT_h, the assumption is made that ΔT_h is polarization independent (i.e., same for v-pol and h-pol). There is good physical and empirical justification for this assumption. Assuming ΔT_h is independent of polarization allows the usage the following linear combination of v-pol and h-pol T_A differences:

$$\delta T_{Ax}(i, j) = \delta T_{Av}(i, j) - \kappa \delta T_{Ah}(i, j) \qquad (33)$$

where the weighting coefficient κ = 0.53. This linear combination is selected because it is very insensitive to variations in the atmosphere moisture (i.e., *V* and *L*). Over the oceans, changes in atmospheric absorption due to either *V* or *L* affect h-pol about twice as much as v-pol, and hence $\delta T_{Ax}(i, j)$ is largely insensitive to these changes. The largest source of error in computing $\delta T_A(i, j)$ is the specification of *V* and *L* for $\mathbf{T_{A,rtm}}(j)$, and using (33) greatly reduces this error. Combining (32) and (33) gives

$$\Delta T_h = \frac{(T_h - T_c)\delta T_{Ax}(i, j)}{T_{Av} - T_c - \kappa(T_{Ah} - T_c)} \qquad (34)$$

Equation (34) cannot be used for the 22 GHz channel because there is only a v-pol measurement. For this case, we use the 19 GHz ΔT_h to specify the 22 GHz value.

Analyses of hot target errors for WindSat [*Twarog et al*., 2006] and SSM/IS [*Sun and Weng*, 2008] indicate that at certain points in the orbit the sun shining on the hot target

produces thermal gradients that are not captured by the thermistors. These events are typically characterized as 'solar intrusions' where the solar radiation either directly or via a reflection impinges onto the hot target. For these events the effective temperature of the hot target is not adequately represented by $T_{h,therm}$. The geometry of the solar intrusions can be complex with both direct and reflected intrusions causing problems. For the SSM/Is, rather than trying to explicitly model the geometry of the intrusions, we simply assume ΔT_h is a function of the sun's azimuth angle α and polar angle β as measured in the spacecraft coordinate system for which the z-axis points up away from nadir and the x-axis is the spacecraft velocity vector. We denote this function by $\Delta T_h(\alpha, \beta)$. Equation (34) is then used to make tables of $\Delta T_h(\alpha, \beta)$.

The derivation of $\Delta T_h(\alpha, \beta)$ requires a pair of collocated SSM/Is, and the pairs used are shown in Table 5. For the F08 SSM/I the only period of overlap is with the F10 SSM/I for one year, and during this year the F10 data have numerous gaps. We decided there was insufficient data to derive $\Delta T_h(\alpha, \beta)$ for F08 and simply set it to zero. The derivation of $\Delta T_h(\alpha, \beta)$ for F10 was problematic. The $\Delta T_h(\alpha, \beta)$ values were considerably larger than found for the other 4 SSM/Is (F11 through F15). Also the F10 $\Delta T_h(\alpha, \beta)$ derived from the different frequencies did not resemble each other nor did the $\Delta T_h(\alpha, \beta)$ derived separately from v-pol and h-pol. The other SSM/Is show similar $\Delta T_h(\alpha, \beta)$ among the various frequencies and polarizations. In addition, we also found that the error for a given region in α,β space varied over the course of the mission, suggesting that other, time-dependent error source are in play for F10. We concluded that the δT_As we are seeing for F10 are mostly do some other effect not related to a hot target error (see Section 3.4.8). Hence we set the F10 $\Delta T_h(\alpha, \beta)$ to zero.

F11 through F15 all show reasonable values for $\Delta T_h(\alpha, \beta)$ that are spectral consistent and range from ±1 K. Since 22 GHz does not have a h-pol channel, $\delta T_{Ax}(i, j)$ cannot be computed. Instead for 22 GHz, we use the 19 GHz $\Delta T_h(\alpha, \beta)$. Since SSM/I employs a single feedhorn, we do not expect $\Delta T_h(\alpha, \beta)$ will depend strongly on frequency. In spite of using the linear combination of v-pol and h-pol, atmospheric noise at the highest frequency of 85 GHz is still somewhat large, and we consider it best to simply set the 85 GHz $\Delta T_h(\alpha, \beta)$ to that found for 37 GHz. Figure 5 shows 19 and 37 GHz hot target adjustments for F11 through F15.

In addition to $\Delta T_h(\alpha, \beta)$, there is a second adjustment that is made to the hot target temperature. This adjustment, which is applied to all SSM/Is, is based on the difference between the evening (pm) and morning (am) T_A measurements, and is denoted by $\Delta T_h(\psi, t)$, where ψ is the spacecraft angular position in orbit and t is time. The angle ψ equals 0 when the spacecraft is at its southern-most position in the orbit. This adjustment is modeled by a small but very systematic error we see between the pm and am measurements that we do not believe is due to real diurnal effects. The $\Delta T_h(\psi, t)$ adjustment is quite small, typically being ±0.2 K, and never exceeds ±0.5 K except at the very end of the missions for F10 and F15. The adjustment takes the form

$$\Delta T_h(\psi, t) = \left[G_0 + G_1(t) + G_{85}(t_{asc}) \right] \sin\psi \qquad (35)$$

where G_0 is a constant that just depends on channel number and $G_1(t)$ is a slowly varying function of time t that is independent of channel number. The last term $G_{85}(t_{asc})$ is a special adjustment only applied to the 85 GHz channels. The derivation of these three terms and an explanation of how they are separated from the natural diurnal variation of $\mathbf{E_p}$ is given in Section 3.4.12.

The two hot target adjustments are then added together to obtain the total correction:

$$\Delta T_h = \Delta T_h(\alpha,\beta) + \Delta T_h(\psi,t) \qquad (36)$$

2.4.7 Closure Tests and the F08 SSM/I Calibration Adjustment

As discussed in Section 3.4.2, a very useful calibration tool is the degree of closure as expressed by (8) or equivalently by (14) with $i = j$. Closure is essentially a consistency test between the calibrated T_A measurements and the geophysical retrievals. Figure 6 shows $\mathbf{\delta T_{A,closure}}$ plotted versus spacecraft orbit position ψ and time for the F13 SSM/I. In addition to v-pol and h-pol, results are shown for the linear combination V-0.53H, which is insensitive to atmospheric variations. Excellent closure results are obtained from the lower-frequency channels, for which the $\mathbf{\delta T_{A,closure}}$ features are of the order of ±0.2 K over all ψ and time. The 85 GHz results show larger features due to the heavy influence of the atmosphere at this highest frequency. In the 85-GHz plot of V-0.53H, these atmospheric related features are substantially reduced, although a small drift over the mission life seems to persist for which we have no explanation.

The other SSM/Is show similarly good closure results except for F08 and F15 after the RADCAL beacon is turned on (see Section 3.4.9). For the F08 SSM/I, $\mathbf{\delta T_{A,closure}}$ shows abrupt changes, as shown in Figure 7 by the vertical bars. The cause of these abrupt changes is unclear. It is hard to imagine either the cold or hot target could change this abruptly. The only explanations we could envision are some type of intermittent RFI or a non-linearity problem with the receivers. We decided to model the effect as a non-linearity problem.

The effect of a receiver non-linearity on T_A can be modeled as follows:

$$\Delta T_{A,F08nl} = \frac{(T_A - T_c)(T_h - T_A)}{(T_{A,ocean} - T_c)(T_h - T_{A,ocean})}\Lambda_{F08}(t) \qquad (37)$$

where $\Lambda_{F08}(t)$ is a measure of the non-linearity in terms of Kelvin. This expression has the required property that the non-linearity has no effect with the scene temperature T_A equals either the cold target or hot target temperature. Since $\Lambda_{F08}(t)$ is derived from rain-free ocean observations, the proper normalization for (37) is obtained by using the global mean ocean antenna temperature $T_{A,ocean}$ in the denominator. The values for $T_{A,ocean}$ are given in Table 7. The non-linearity adjustment is not sensitive to the exact values used for $T_{A,ocean}$ because any change in for $T_{A,ocean}$ would be mostly be compensated for by a change in the derived value of $\Lambda_{F08}(t)$.

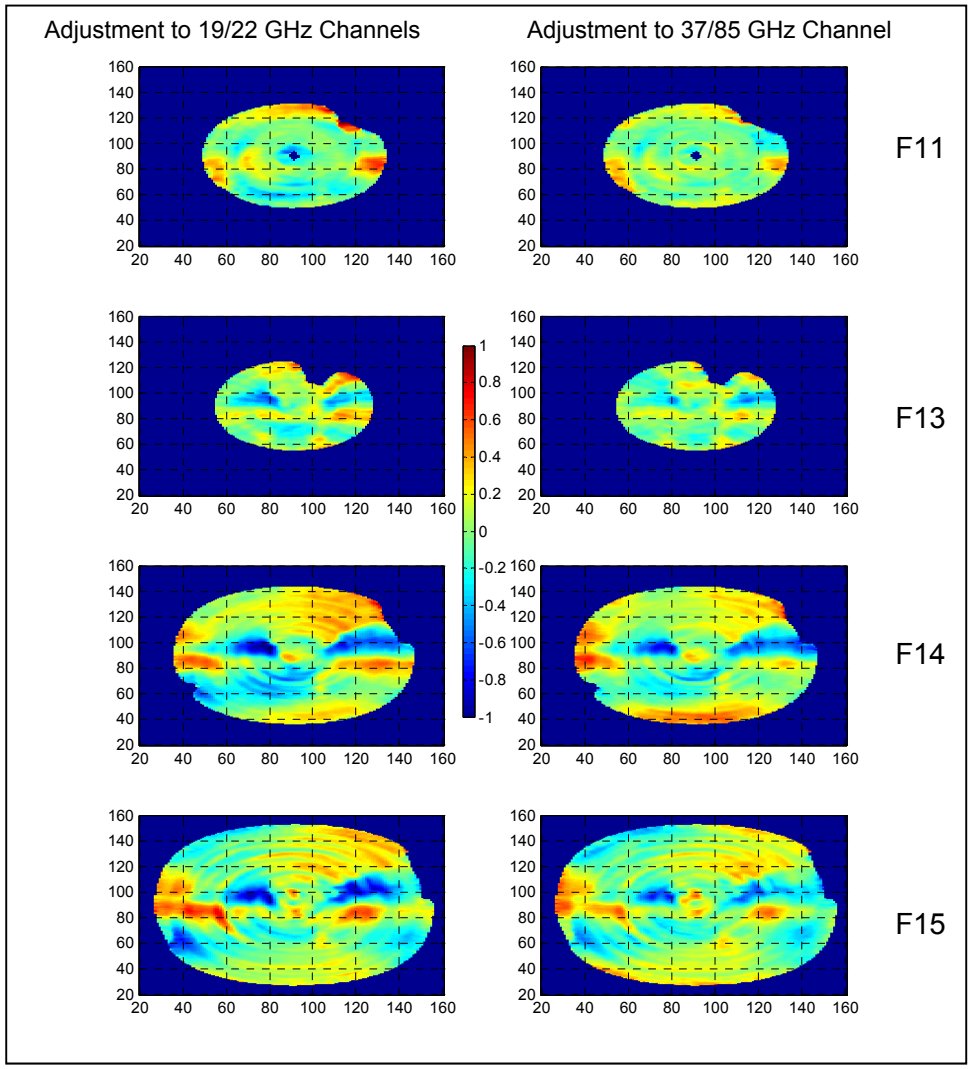

Figure 5. Adjustment to the hot target temperature $\Delta T_h(\alpha, \beta)$ to account for solar heating of the hot target. The two columns correspond to the adjustment applied to the 19/22 GHz channels and the 37/85 GHz channels. The 4 rows correspond to F11 through F15. This adjustment is not used for F08 and F10. The x-axis is the sun azimuth angle α and the y-axis is the sun zenith angle β relative to spacecraft coordinates. The color bar goes from −1 K to +1 K.

An analysis of the results in Figure 7 reveals that the 19 GHz channels are the primary cause of the problem. The problem seen at 37 GHz is due to the T_A errors in the 19 GHz channels producing errors in the cloud water retrievals, which are then used to compute the RTM T_A at 37 GHz. This conclusion is supported by the fact that the 37 GHz V-0.53H plot is relatively free of error features. As indicated by (37), the non-linearity is represented as a simple function of just time, and we assume only the 19 GHz channels are affected. The $\Lambda_{F08}(t)$ timeseries for 19V and 19H are found by setting $\Delta T_{A,F08nl}$ to $\mathbf{\delta T_{A,closure}}$, and then inverting (37) to give $\Lambda_{F08}(t)$. Figure 8 shows the results.

This non-linearity correction is the only sensor-specific adjustment we apply to F08 and hence

$$\Delta T_{A,F08} = \Delta T_{A,F08nl} \tag{38}$$

Table 7. Calibration Parameters Depending Just on Channel Number

	19V	19H	22V	37V	37H	85V	85H
Globally Averaged Ocean T_A (K)	191	115	216	209	154	252	222
F10 EIA Correction Coeff. μ (K/deg)	−0.0306	0.0647	−0.1255	−0.0012	0.0978	−0.0114	0.0455
F15 RADCAL Offsets H_0 (K)	−0.05	0.25	−0.31	0.08	0.46	0.18	0.68

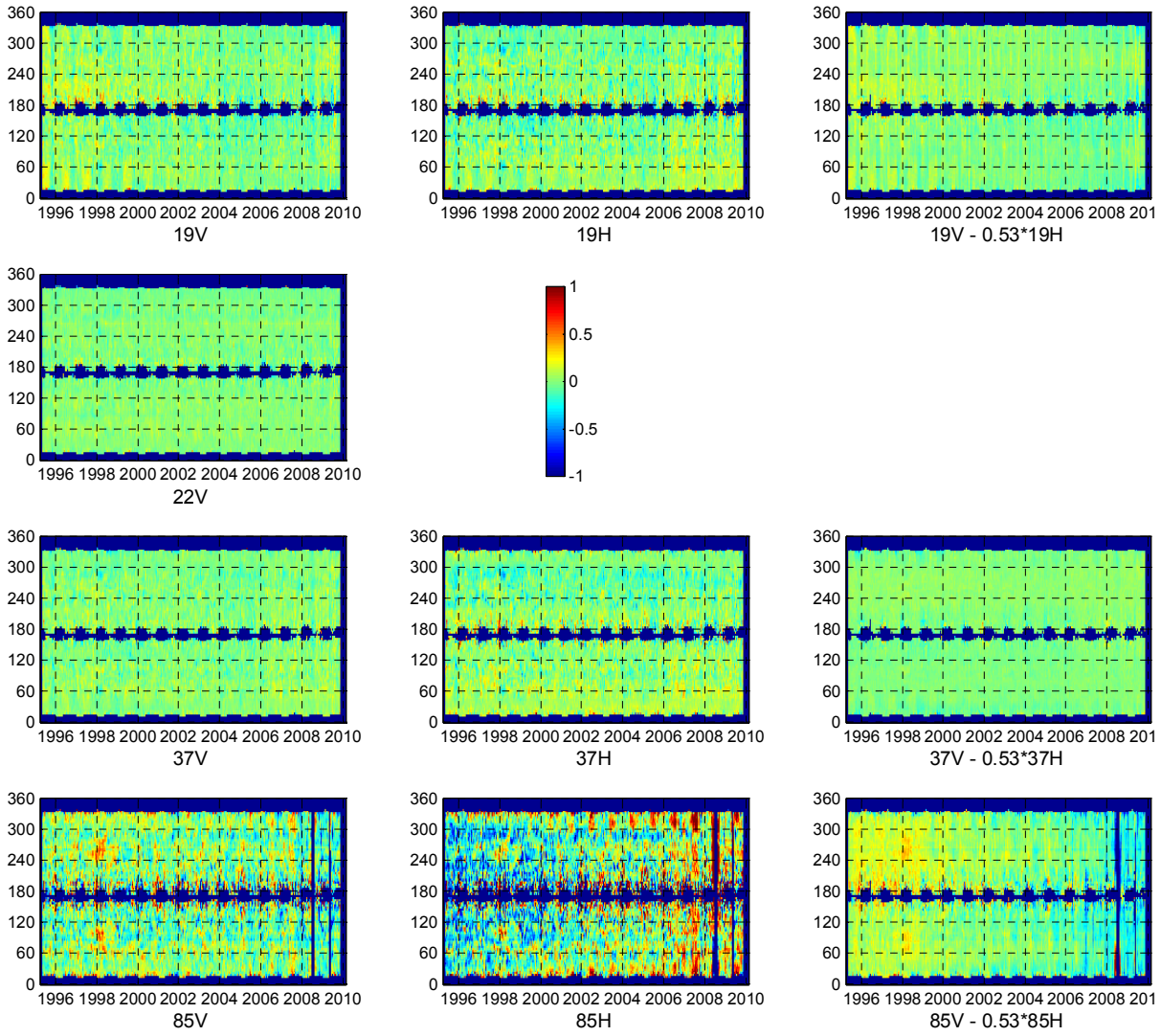

Figure 6. The F13 SSM/I closure residual $\delta T_{A,closure}$ (K) plotted versus spacecraft orbit position ψ (y axis) and time (x-axis) for v-pol (first column), h-pol (second column), and the linear combination V-0.53H (third column), which is insensitive to atmospheric variations. The color bar goes from −1 K to + 1 K.

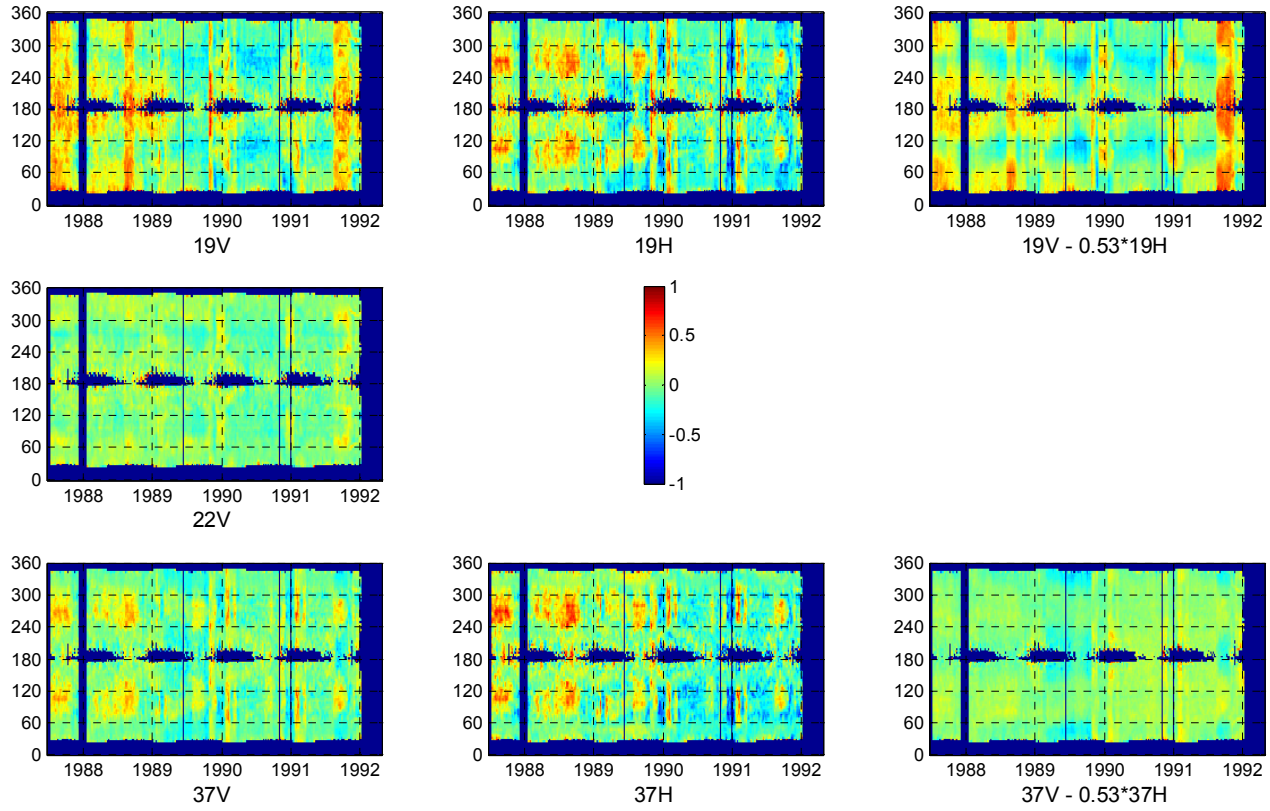

Figure 7. The F08 SSM/I closure residual $\delta T_{A,closure}$ (K) plotted versus spacecraft orbit position ψ (y axis) and time (x-axis) for v-pol (first column), h-pol (second column), and the linear combination V-0.53H (third column), which is insensitive to atmospheric variations. The color bar goes from −1 K to + 1 K. The 85 GHz channel is not shown because these channels failed for F08. The vertical bars in the 19V and 19H plots indicate a calibration error for F08.

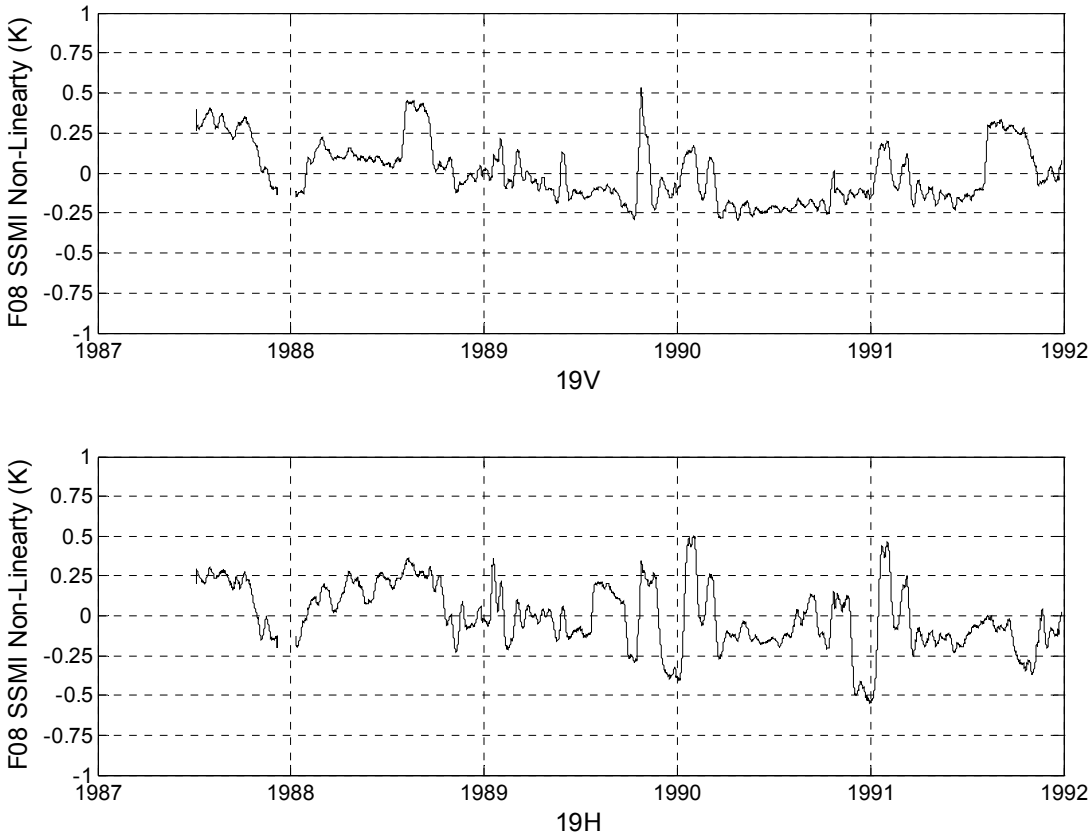

Figure 8. The F08 SSM/I non-linearity correction $\Lambda_{F08}(t)$ (K) plotted versus time for the two 19 GHz channels.

2.4.8 Calibration Adjustments Specific to the F10 SSM/I

Due to a malfunction in the launch of F10, the spacecraft did not end up in the desired orbit. Its orbit was more elliptical than the other SSM/Is. Also the internal temperature of the electronics, as measured by a thermistor, was unusually high. After some erratic fluctuations during the first few months after launch, the temperature of the electronics stabilized to a range between 318 and 326 K (see Figure 3A in the Appendix). This is considerably hotter than the other SSM/Is, which have an internal temperature around 300 K. The one exception is the F08 SSM/I, for which the internal temperature each December rises to about 320 K, and this unanticipated rise in temperature damaged the F08 85-GHz receivers. Subsequent to F08, the thermal insulation around the sensor was adjusted to eliminate this heating problem. We assume that the very hot temperature experienced by F10 is due to its anomalous orbit.

As discussed in Section 3.4.6, the errors in the F10 observations did not look like hot target errors, and we seek to find some other explanation. One possible cause of the F10 T_A errors is the receivers are not functioning as designed due to their high temperature. Possibly, some of the F10 receivers degraded in such a way that they no

longer have a linear response function. There is no way of telling for sure, but this was the only hypothesis we could find to explain the F10 T_A errors. So we use the same non-linearity model (37) that was used in Section 3.4.7 for F08.

$$\Delta T_{A,F10nl} = \frac{\left(T_A - T_c\right)\left(T_h - T_A\right)}{\left(T_{A,ocean} - T_c\right)\left(T_h - T_{A,ocean}\right)} \Lambda_{F10}\left(\psi, t\right) \qquad (39)$$

where $\Lambda_{F10}(\psi,t)$ is the non-linearity error function for F10 and is a function of the spacecraft orbit position ψ and time t.

Following the procedure described in Section 3.4.5 and 3.4.6, the assumption is made that $\delta T_A(i, j) = \Delta T_{A,F10nl}$ and (39) is inverted to yield $\Lambda_{F10}(\psi,t)$. A tables of $\Gamma_{F10}(\psi,t)$ are thus made. For $\delta T_A(i, j)$, we used both the (F10, F08) pair and the (F10, F11) pair so as to cover the complete F10 mission. When the $\Lambda_{F10}(\psi,t)$ maps were first made, some of the features looked very much like water vapor V and cloud liquid water L artifacts. The F10 SSM/I local observation time is about 3 hours later in the day than the F08 and F11 SSM/Is, and hence the collocation is not that good. Errors δV and δL in specifying V and L for F10 will produce errors in $\delta T_A(i, j)$. Assuming that part of the $\delta T_A(i, j)$ difference is due to δV and δL, we developed a simple linear retrieval algorithm that finds δV and δL so as to minimize the variance of $\delta T_A(i, j)$ over the 7 channels. These δV and δL errors are then removed from $\delta T_A(i, j)$. This analysis indicated that nearly all the features seen in the original 19H and 37H $\Lambda_{F10}(\psi,t)$ maps are due to δV and δL, and $\Lambda_{F10}(\psi,t)$ is set to zero for these 2 channels. Figure 9 shows $\Lambda_{F10}(\psi,t)$ for the other 5 channels, having first removed the δV and δL errors. The 85H channel looks particularly bad; reminiscent of the problem experienced by the F08 SSM/I 85 GHz channels, which also operated at a very hot temperature.

There is one other adjustment that is made to the F10 SSM/I. This adjustment relates to the F10 elliptical orbit. The angle of perigee of the F10 orbits has a fixed period of 122 days over the course of the mission. As a result, the Earth incidence angle θ_i for F10 also exhibits a 122 day cycle (see Figure 4A in the Appendix). For the two equator crossings (ascending and descending), the following expression holds

$$\theta_i = \theta_{io} \pm 0.6 \cos\left(\frac{360^o\left(t_{day} - t_o\right)}{122}\right) \qquad (40)$$

where θ_{io} is the nominal incidence angle, t_{day} is time in terms of days, and t_o is the phase. The plus sign is for the ascending crossing and the minus sign is for the descending crossing. Hence the ascending minus descending θ_i difference has a very strong 122-day modulation of 1.2^o.

An analysis of the F10 T_A's and geophysical retrievals, particularly vapor, reveals ascending minus descending differences that had a periodicity of 122 days. Even though these T_A and EP differences are very small, they could be clearly detected due to their fixed harmonic nature. Possibly the RTM and geophysical retrieval algorithm are not modeling the Earth incidence angle (EIA) effect precisely enough. We found

that adding the following second term to the F10 T_A adjustment completely corrected the problem:

$$\Delta T_{A,F10} = \Delta T_{A,F10nl} + \mu\left(\theta_i - \theta_{io}\right) \tag{41}$$

where the μ coefficient is found by regression and is given in Table 7. The magnitude of this correction is about ±0.04 K except that the 22V channel is larger being ±0.08 K.

The F10 elliptical orbit provides the means to assess the accuracy of RTM EIA functionality. For v-pol, the derivative $\partial T_A/\partial\theta_i$ is about 2 K/deg. Hence the 122-day modulation of 1.2° corresponds to a 2.4 K modulation in T_A. The maximum residual error in modeling this modulation is 0.08 K. This indicates the RTM is modeling the EIA effect to an accuracy of 3%, or better.

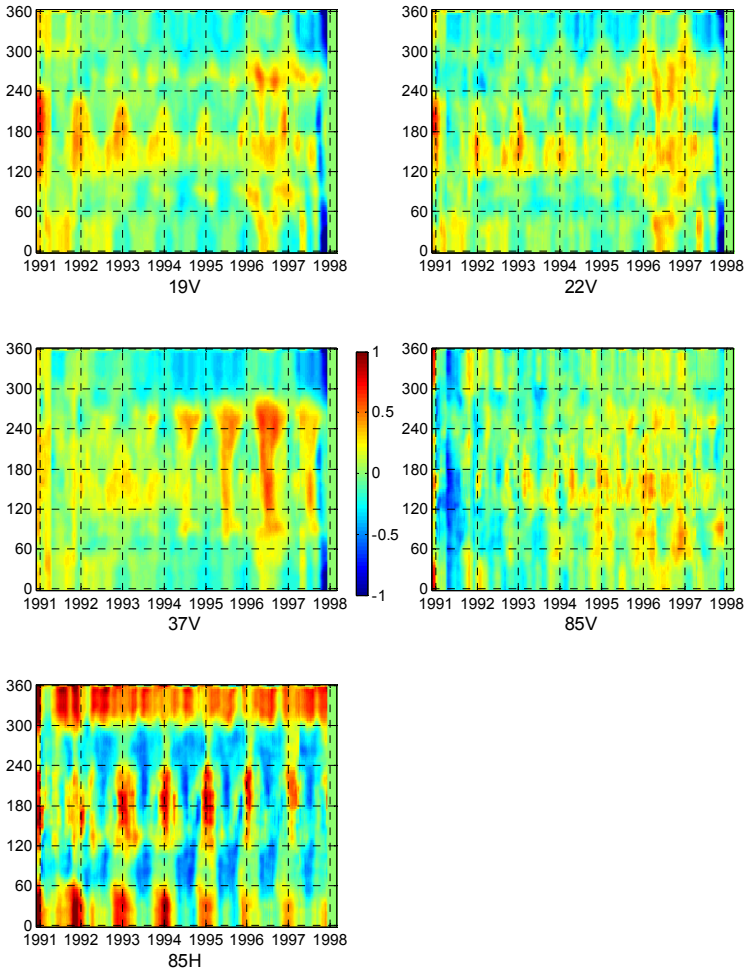

Figure 9. F10 non-linearity adjustment $\Lambda_{F10}(\psi,t)$ applied to 19V, 22V, 37V, and both 85 GHz channels. The x-axis is time and the y-axis is spacecraft orbit position ψ. The color bar goes from −1 K to +1 K

2.4.9 Adjustment for the F15 RADCAL Beacon

On 14 August 2006, a radar calibration beacon (RADCAL) was activated on F15. This radar interfered with the SSM/I, primarily the 22V channel. We apply a correction to the F15 SSM/I to mitigate the RADCAL interference. This correction was derived by *Hilburn and Wentz* [2008] and *Hilburn* [2009] and is given by

$$\Delta T_{A,F15} = H_0 + H_1(\omega)\left(79.8977 - 0.518557 t_h + 8.51691\times10^{-4} t_h^2\right) \qquad (42)$$

where ω is the along-scan position angle and t_h is the average temperature of the 3 thermistor readings attached to the hot target. H_0 are small offsets that are applied to the each channel and are given in Table 7. $H_1(\omega)$ is only applied to the 22 GHz channel and is a table of 64 values corresponding to the SSM/I scan positions. $H_1(\omega)$ is shown in Figure 10. When computing (42), if t_h falls outside the range 250 to 298 K, it is set to 250 or 298 K. The offsets H_0 are found by looking at $\delta T_A(15, 13)$ before and after the beacon was turned on.

The RADCAL correction was found some time ago and can be improved upon using closure analysis. Figure 11 shows the closure residual $\mathbf{\delta T_{A,closure}}$ plotted versus spacecraft orbit position ψ and time for F15. This figure is analogous to Figures 6 and 7. Excellent closure results are obtained up until the RADCAL beacon is turned on. Then, the interference from the beacon produces closures errors of the order of ±1 K. Most of the closure errors shown in Figure 11 are due the 22V channel not being fully corrected, and as a result there are errors in the vapor retrievals, which in turn affect the $\mathbf{\delta T_{A,closure}}$ for all channels. This hypothesis is supported by the fact that the V-0.53H closure results, which are insensitive to vapor, show little error. These results indicate more calibration work is required for F15, and until this is done, some caution should be exercised when using the post-RADCAL F15 retrievals for climate research.

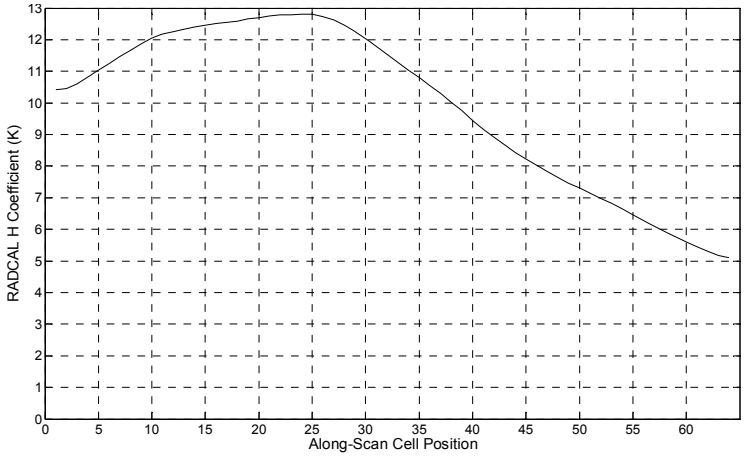

Figure 10. The RADCAL $H_1(\omega)$ function plotted versus scan position.

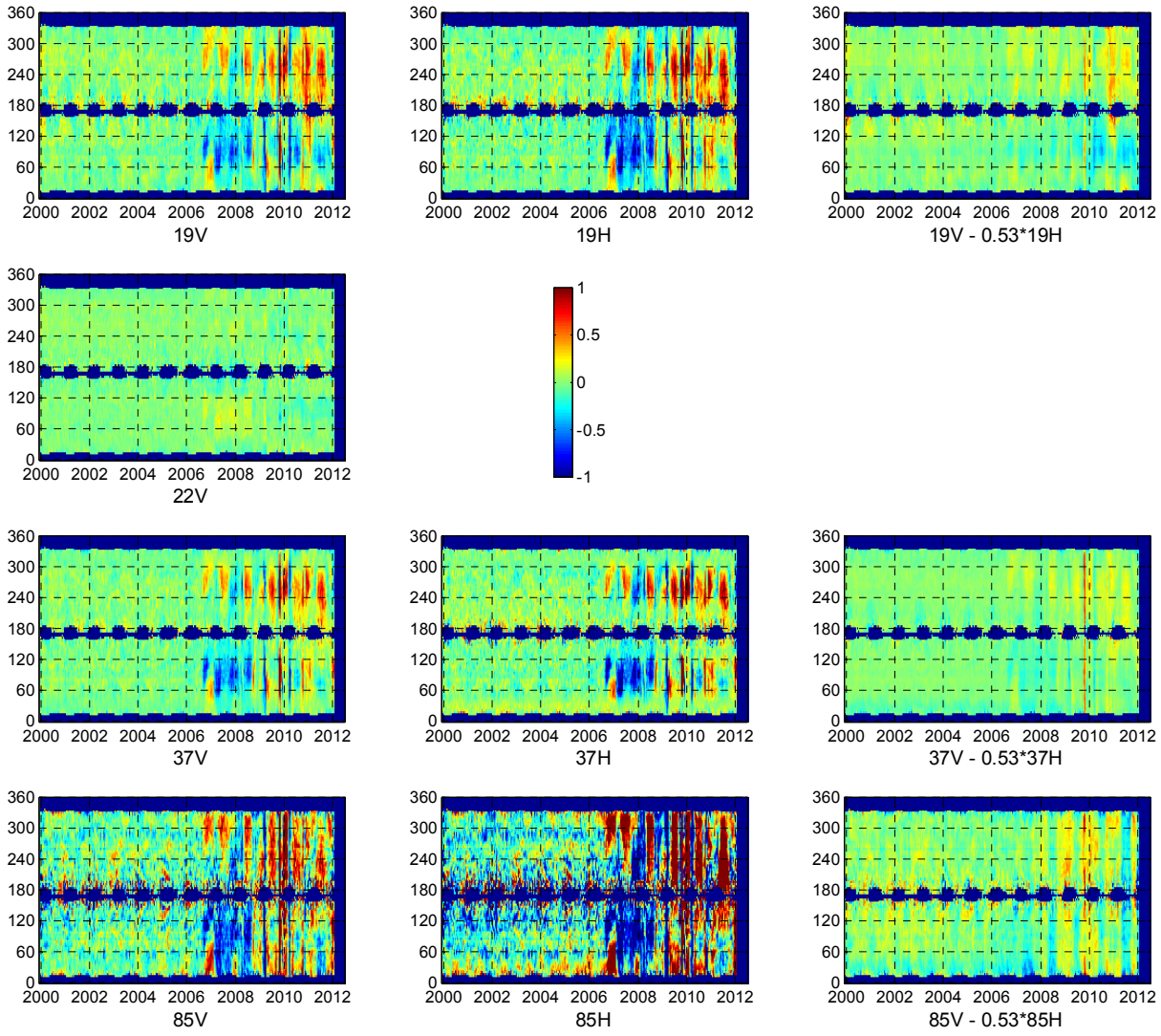

Figure 11. The F15 SSM/I closure residual $\delta T_{A,closure}$ (K) plotted versus spacecraft orbit position ψ (y axis) and time (x-axis) for v-pol (first column), h-pol (second column), and the linear combination V-0.53H (third column), which is insensitive to atmospheric variations. The color bar goes from −1 K to + 1 K. In August 2006, the RADCAL beacon was turned on, and at this point the closure residuals become large.

2.4.10 Early Mission Time Drift Corrections for the F11 and F13 SSM/I

There are two indications that the F11 SSM/I T_As exhibited a small drift during the first two years of the mission. The primary indication is that the F11 wind speed retrievals for the first two years were low relative to collocated scatterometer wind speeds obtained from the ERS-1 satellite. This is further supported by a completely separate analysis looking at histograms of wind speed retrievals from F11. This analysis showed a slight negative shift of the left edge of the histograms (i.e., the position of the histogram for wind=0) for the first two years relative to the rest of the F11 mission. The second indication of a small drift is that the F11 vapor retrievals were slightly high relative to the F10 vapor retrievals during the first two years of overlap between the two satellites. These effects were largest during the first year (−0.2 m/s in wind and +0.1 mm in vapor), and then reduced in the second year, and were barely noticeably in the third year. Direct comparisons of the F11 T_As with F10 seemed to suggest the problem was with the F11 37 GHz channels, albeit F10 has its own calibration problems. We experimented with different ways to adjust the T_As, and found the simplest and smallest adjustment that would fix both the wind and vapor drift is the following

$$\Delta T_{A,drift,F11} = \pm 0.15 \left(\frac{1995 - t_{year}}{3} \right)^{1.5} \tag{43}$$

where this adjustment is just applied to the 37 GHz channels and the plus (minus) sign is used for 37V (37H). The adjustment is only applied prior to 1995. The adjustment is quite small, being a maximum of ±0.15K when F10 began operation in December 1991. After 1994, extensive cal/val activities indicate the F11 SSM/I is very stable.

The F13 SSM/I began operation in May 1995. Previous comparisons of the early mission F13 T_As with the F11 T_As showed slow time variations in the difference, but only during the first 18 months of F13 operation. These F13-F11 T_A differences are hard to explain. In general, F13 seems to be stable and well calibrated. Except for the first 18 months, the F11 and F13 SSM/Is track each other extremely well. We elected to assign the problem to F13 assuming it was some sort of early mission stabilization. The *Wentz* [2010] correction is shown in Figure 12 and is small being −0.1 to +0.2 K at the begin of the mission The more recent analysis presented herein supports this previous finding, and we use the *Wentz* [2010] correction to specify $\Delta T_{A,drift}$ for F13.

Rather than assigning the time drift to F13, we could have applied it to F11. This is an example of sensor error crosstalk discussed in Section 3.4.2. In this case, there is no definitive way to assign the error to one sensor or the other. We somewhat arbitrarily assume it is an early mission problem for F13.

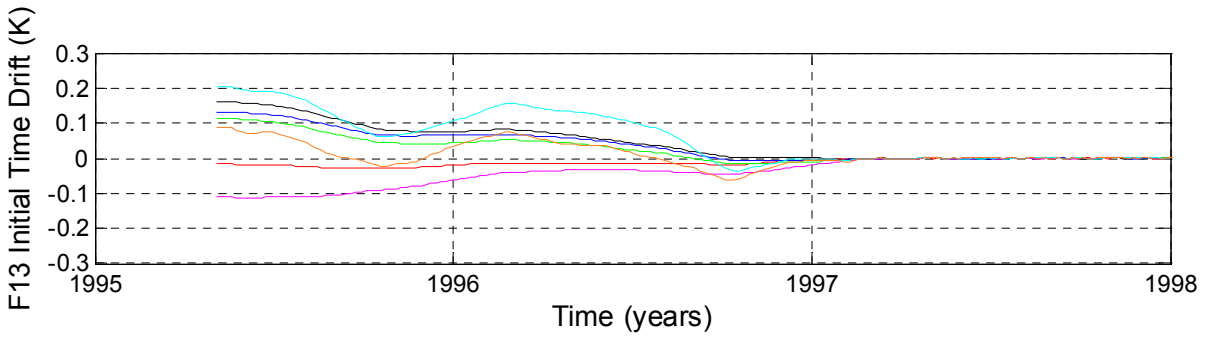

Figure 12. Early mission time drift $\Delta T_{A,drift}$ for the F13 SSM/I. The 7 colors correspond to the 7 channels as indicated in Table 6.

2.4.11 Target Factor Adjustment

The idea of the 'target factor' adjustment comes from calibration work done for NOAA's Microwave Sounding Unit (MSU) and the Advanced Microwave Sounding Unit (AMSU). The MSU and AMSU are atmospheric profilers that measure air temperature in different layers of the atmosphere. Much work has gone into the inter-satellite calibration of this series of MSU/AMSU that starts in 1979. In many aspects, this calibration work is similar to that discussed herein. One finding from the MSU investigations is that inter-satellite offsets are correlated with the hot-target temperature [*Christy et al.*, 2000; *Mears et al.*, 2003]. It is not clear why such a correlation exists, but possibly it is related to non-linearities in the radiometer response function. We include this target factor term in our SSM/I error model to see if it explains some of the observed inter-satellite T_A variation. This term is given by

$$\Delta T_{A,tf} = \xi\left(T_h - \langle T_h \rangle\right) \tag{44}$$

where ξ denotes the target factors and $\langle T_h \rangle$ is the mission-averaged hot-target temperature, which is given in Table 8.

The target factors are found by solving a set of simultaneous linear equations, similar to that described by *Mears et al.* [2003]. The T_A measurements are first adjusted to remove all error terms other than $\Delta T_{A,tf}$. These adjusted T_As are then normalized to a common incidence angle and antenna function and the dependency on wind direction is removed as is specified by equations (9) and (10). Inter-satellite differences of these normalized T_As as defined by (15) are then:

$$\delta T_A'(i,j) = \xi_j\left(T_{hj} - \langle T_{hj} \rangle\right) - \xi_i\left(T_{hi} - \langle T_{hi} \rangle\right) \tag{45}$$

All 11 pairs of inter-satellite overlaps show in in Table 2 are used to solve (45). Thus, for a given channel number, (45) represents 11 simultaneous timeseries. The target factors are found via standard least-squares estimation so as to minimize the overall

variance of $\delta T'_A(i, j)$. There is too little variation in the F10 T_h (±9 K) to reliably find ξ_{F10} (see Figure 1A in the Appendix). So the F10 target factor is constrained to be zero. Also on F08, the 85 GHz channels failed, and these target factors also constrained to be zero. Table 8 gives the target factors for all 6 SSM/Is and 7 channels.

For the MSU analyses [*Mears et al*., 2003], several sensors had ξ values of 3%. However, for the SSM/Is the largest ξ value is about 1%, except for the F15 37H and 85V channels, which have a somewhat higher ξ. These higher target factors for F15 are possibly an artifact of residual RADCAL problems. For the most part ξ is below the 1% level. This suggests the target-factor effect is not as serious of a problem for SSM/I as it is for MSU.

These V7 target factors are a little different than the Version 6 values given by *Wentz* [2010]. One reason for the difference is that for V7 we apply the offsets δT_c and δT_h to T_c and T_h. It can be shown that applying such offsets to the calibration targets directly impact the estimation of ξ. The application of δT_c and δT_h increases the estimated value of ξ by about 0.003. As a result nearly all of the V7 target factors are positive, with 3 minor exceptions (see Table 9). Accounting for the 0.003 change, the typical differences between the V6 and V7 ξ is about 0.001 (maximum difference is 0.003), with the exception of F15. The V6 calibration only used data through mid-2006. During this period the F15 T_h exhibited very little variation (±7 K), and it was difficult to get a reliable estimate for ξ. After 2006, the F15 T_h exhibited much more variation (±25 K), and a better estimate of ξ could be obtained when doing the V7 calibration.

Table 8. Mission-Averaged Hot Target Temperatures $<T_h>$ (K) and Target Factors ξ

	F08	F10	F11	F13	F14	F15
$<T_h>$	263.23	306.49	277.02	291.04	301.41	298.06
19V ξ	0.0008	0	−0.0016	0.0060	0.0051	0.0094
19H ξ	0.0051	0	0.0007	0.0053	0.0034	0.0113
22V ξ	0.0047	0	0.0023	0.0073	0.0070	0.0091
37V ξ	−0.0016	0	0.0031	0.0071	0.0063	0.0082
37H ξ	−0.0044	0	0.0032	0.0117	0.0114	0.0213
85V ξ	0	0	0.0029	0.0066	0.0082	0.0150
85H ξ	0	0	0.0041	0.0105	0.0115	0.0095

2.4.12 Comparison of Evening and Morning T_A

A standard calibration analysis tool is to compare ascending (asc) versus descending (dsc) T_A measurements at the same location on the Earth. As Figure 1 shows, the local

time for the SSM/Is' ascending equator crossing is between 5 and 10 pm, depending on satellite and mission time. The one exception is the F08 SSM/I, which has a 6 am ascending node time. To compare the asc and dsc T_A measurements, we use a 1° latitude-longitude grid with a temporal resolution of 5 days (pentads). The measurements are pre-averaged onto this grid. The collocation requirement is that a given 1° pentad grid cell contains both an asc and dsc measurement.

We consider 3 parameters that may be responsible for systematic asc minus dsc differences: liquid water in clouds *L*, water vapor *V*, and error in specifying the hot target temperature T_h. The major contributor is cloud cover, which peaks in the early morning. The variation of these parameters relative to their mean value over the course of an orbit can be represented by a Fourier series in terms of the spacecraft orbit position ψ:

$$F(\psi) = \sum_{n=1}^{\infty} G_n \sin n\psi + H_n \cos n\psi \qquad (46)$$

For a given 1° grid cell containing an asc and dsc observation, let ψ_{asc} denote the orbit position angle for the asc observation. The orbit position angle for the dsc observation is then

$$\psi_{dsc} = 360 - \psi_{asc} \qquad (47)$$

Hence the asc minus dsc difference of a given parameter within a 1° grid cells is

$$F(\psi_{asc}) - F(\psi_{dsc}) = 2\sum_{n=1}^{\infty} G_n \sin n\psi_{asc} \qquad (48)$$

Averaging these 1° grid cell differences over all latitudes and longitudes gives

$$\left\langle F(\psi_{asc}) - F(\psi_{dsc}) \right\rangle = 2\sum_{n=1}^{\infty} G_n \left\langle \sin n\psi_{asc} \right\rangle \qquad (49)$$

where the brackets denote the average. The latitudinal averaging will tend to diminish the higher order terms, and we approximate the asc minus dsc difference to first order as $2G\langle \sin \psi_{asc} \rangle$. Hence, the analysis of asc−dsc differences only allows us to determine the amplitude of the sin ψ term. The other terms in the Fourier series are not considered herein.

Since the F08 SSM/I has an ascending node that is about 12 hours shifted from the other SSM/Is, it is more convenient to work in terms of evening versus morning (i.e. pm versus am) differences than asc versus dsc. By defining the F08 orbit position angle relative to it descending node (i.e., $\psi \leftarrow 360 - \psi$), one can treat all SSM/Is in a consistent manner. Switching notation from asc,dsc to pm,am, the pm−am T_A difference is given by.

$$T'_{A,pm} - T'_{A,am} = 2\left\{ \frac{\partial T_A}{\partial V} G_{vap}(t) + \frac{\partial T_A}{\partial L} G_{cld}(t) + \frac{\partial T_A}{\partial T_h} G_{thot}(t) \right\} \left\langle \sin \psi_{pm} \right\rangle \qquad (50)$$

where $T'_{A,pm}$ and $T'_{A,am}$ are the evening and morning globally averages. The prime symbol denotes that these T_A measurements are normalized to a common incidence angle and the wind direction dependence is removed according to equations (9) and (10). Also, all T_A adjustments are applied except of course the $\Delta T_h(\psi,t)$ adjustment (eq. 35), which is currently being found. The partial derivatives of T_A with respect to V and L are assumed to be fixed values only depending on SSM/I channel number. They represent average global values. The partial derivative of T_A with respect to T_h is given by equation (31). The term $\langle \sin\psi_{pm} \rangle$ is the average of sin ψ_{pm} over all latitudes and is approximately equal to 0.85. Note that because only ocean observations are used, the range of ψ_{pm} is typically between 30° and 150°.

Analysis of the hot target term G_{thot} indicates the data is well fit by the following error model

$$G_{thot}(t) = G_0 + G_1(t) + G_{85}(t_{asc}) \qquad (51)$$

where G_0 is a constant that just depends on channel number and $G_1(t)$ is a slowly varying function of time t. The same $G_1(t)$ is used for all channels. The last term $G_{85}(t_{asc})$ is only applied to the 85 GHz channels. The 85 GHz channels display a time variation slightly different than the lower-frequency channels, and this difference is related to the spacecraft ascending node time t_{asc} (hours):

$$G_{85}(t_{asc}) = 0.3\left\{1 - \cos\left[15(t_{asc} - 22)\right]\right\} \qquad (52)$$

$G_{85}(t_{asc})$ is a very minor term that vary slowly varies over the course of the mission. Its effect is largest for the F15 SSM/I, for which t_{asc} drifted 6 hours over the course of the mission.

Equation (50) does not consider the possibility of systematic SST and wind diurnal features. At the SSM/I frequencies, the dependence of T_A on SST is weak, and when globally averaged, SST diurnal features at the SSM/I am and pm observation times are quite small (< 0.05 C), and in term of T_A this is a <0.02K effect. Hence, we do not think neglecting SST is a problem. We also expect wind diurnal features to be very small when globally averaged [*Smith et al.*, 2002]. By limiting the number of parameters to just 3 (V, L, and T_h), we have a tractable estimation problem because the spectral and polarimetric signatures of the 3 parameters are quasi-orthogonal.

The pm−am T_A differences are regressed to equation (50), and values for G_{vap}, G_{cld}, and G_1 are found for each pentad during a SSM/I mission, thereby finding the timeseries $G_{vap}(t)$, $G_{cld}(t)$, and $G_1(t)$. These timeseries are independent of channel number. The term G_0, which is also found via regression, depends on channel but not on time. The estimation of these parameters is done by standard least-squares so as to minimize the variance between the pm−am T_A differences and the model given by (50). To avoid singularity, a constraint needs to be applied to one of the G_0. We arbitrarily choose to constrain the 37H G_0 to be zero. After completing the regressions for the lower frequency channels, the special 85-GHz term $G_{85}(t_{asc})$ is found by inspection.

The time series for $G_1(t)$ is shown in Figure 13, and the G_0 values are given in Table 9. We note that there are some small differences between the v-pol and h-pol values for G_0. At 19 GHz, the v-pol versus h-pol difference ranges from 0.2 to 0.4 K. At the other frequencies, the difference was always less than 0.15 K. We could not explain these differences via natural diurnal variability nor via hot target error, which is assumed to be independent of polarization. Although we are not sure of the source of the error, it is convenient to lump it with the hot target adjustments.

Our primary motivation of doing the pm versus am T_A comparisons is for sensor calibration. However, the results relating to the diurnal variation of vapor and cloud, i.e., $G_{vap}(t)$ and $G_{cld}(t)$, are very interesting. The time series for $G_{vap}(t)$ and $G_{cld}(t)$ are shown in Figure 14 and 15, respectively. $G_{vap}(t)$ shows a small diurnal effect for which the pm vapor is slightly higher (0.1 mm) than the am vapor. In contrast, $G_{cld}(t)$ shows that clouds have significant diurnal variation with the am cloud being about 0.005 mm higher than the pm cloud when the ascending node time is near 6 pm. We find that the following two simple diurnal models explain the variation shown by the observations:

$$G_{vap}(t) = 0.13\cos\left[15\left(t_{hour}+5\right)\right] \tag{53}$$

$$G_{cld}(t) = 0.008\cos\left[15\left(t_{hour}-3\right)\right]\left\{1+0.2\cos\left[30\left(t_{mon}+1\right)\right]\right\} \tag{54}$$

where t_{hour} is local time of day in terms of hours and t_{mon} is time of year in terms of months. These models are shown by the red curves in Figures 14 and 15. The cloud diurnal cycle given by (54) is very similar to the one we obtained from an analysis of cloud retrievals coming from the TRMM Microwave Imager (TMI). TMI processes through the diurnal cycle every 46 days, and hence provides good sampling for inferring diurnal changes in the environmental parameters. Both (54) and TMI show similar diurnal amplitudes of 0.008 (SSMI) to 0.009 (TMI) with the clouds peaking around 3 am (SSM/I) to 4 am (TMI). The seasonal variation in the amplitude of $G_{cld}(t)$ (i.e., the trailing term in the braces) indicates that the globally averaged diurnal amplitude depends on time of year, reaching a peak in the late fall (December 1). The fact that our am versus pm analysis yields what appears to be an accurate representation of the cloud diurnal cycle provides confidence that the $G_1(t)$ term is indeed a calibration error probably related to solar geometry rather than an artifact of natural diurnal variability.

The vapor diurnal cycle given by (53) is very small. In terms of T_A, the vapor diurnal amplitude is about 5 times smaller than that for cloud. Furthermore when looking at Figure 14, the dependence of $G_{vap}(t)$ on t_{hour} is not obvious other than pm is in general greater than am. Also, the TMI vapor retrievals showed no apparent diurnal dependence. So we would advise caution in over interpreting the small vapor diurnal cycle coming from this analysis.

Figure 16 shows the effect that the calibration adjustments have on the pm minus am T_A differences. The top frame shows the results before applying the adjustments, and the bottom frame shows the improvement obtained when the adjustments are applied. In both case, the diurnal vapor and cloud signals $G_{vap}(t)$ and $G_{cld}(t)$ are first removed.

These are real signals that need to be removed when assessing calibration performance. We also apply the F15 RADCAL beacon correction (42) to both cases. Otherwise, the unadjusted 22V results for the F15 SSM/I would be way off scale. Figure 16 shows that there are still some residual errors in the F15 22V channel due to the RADCAL beacon. As discussed in Section 3.4.9, some more calibration work is required for F15, and until this is done, some caution should be exercised when using the F15 retrievals for climate research. Figure 16 also shows an unexplained anomaly in 85H channel for the F13 SSM/I in 2008. Otherwise, the adjusted results show good pm versus am agreement.

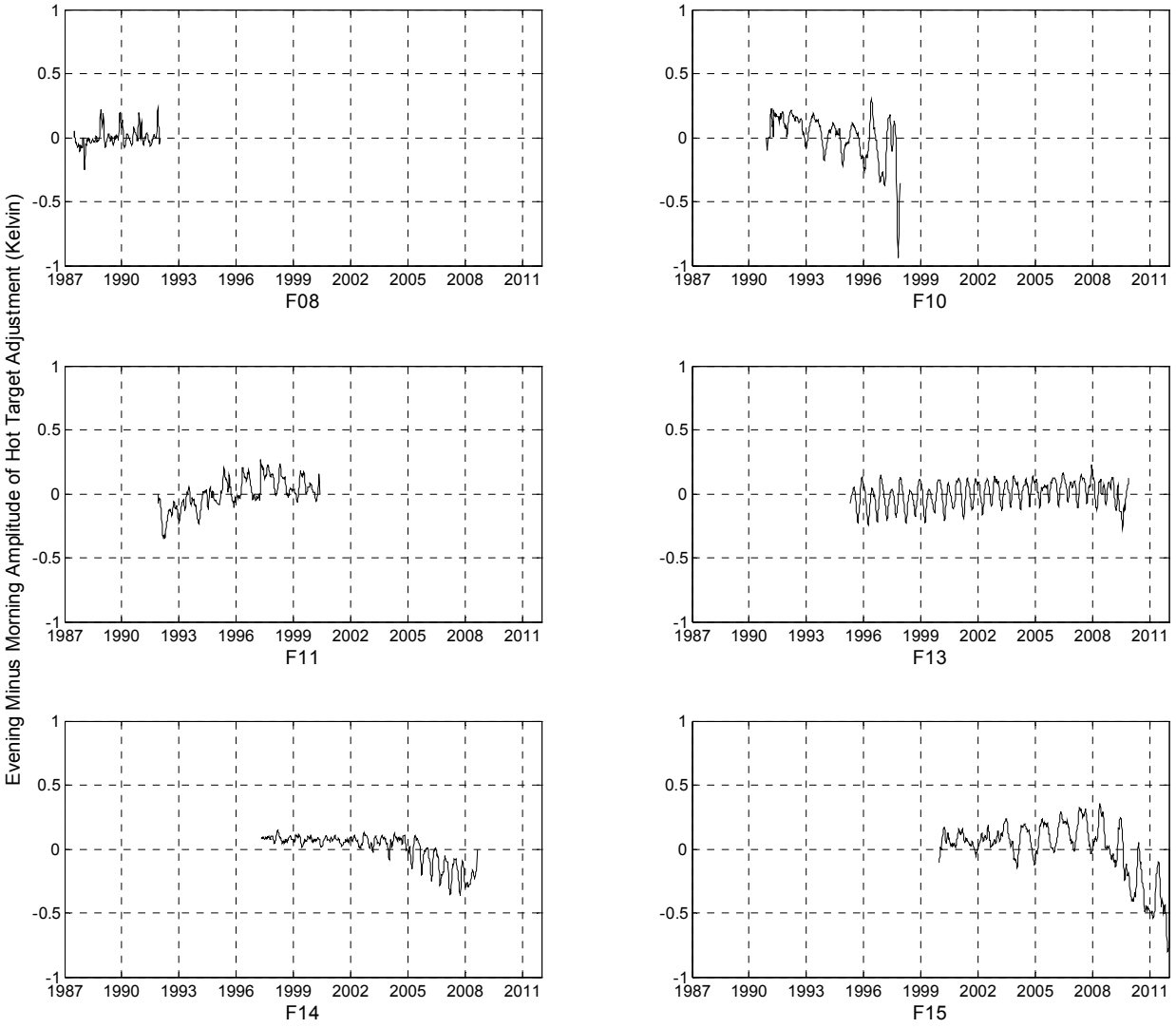

Figure 13. Evening minus morning amplitude of the hot target temperature: $G_1(t)$.

Table 9. Amplitude G_0 (K)

	19V	19H	22V	37V	37H	85V	85H
F08	0.05	-0.08	0.08	0.06	0.00	0.00	0.00
F10	0.24	-0.17	0.00	0.03	0.00	0.09	-0.07
F11	0.02	-0.13	0.03	-0.01	0.00	0.08	0.17
F13	0.02	-0.13	0.05	0.09	0.00	0.07	0.10
F14	0.12	-0.16	0.05	0.15	0.00	0.09	-0.02
F15	0.08	-0.13	0.01	0.12	0.01	0.08	-0.07

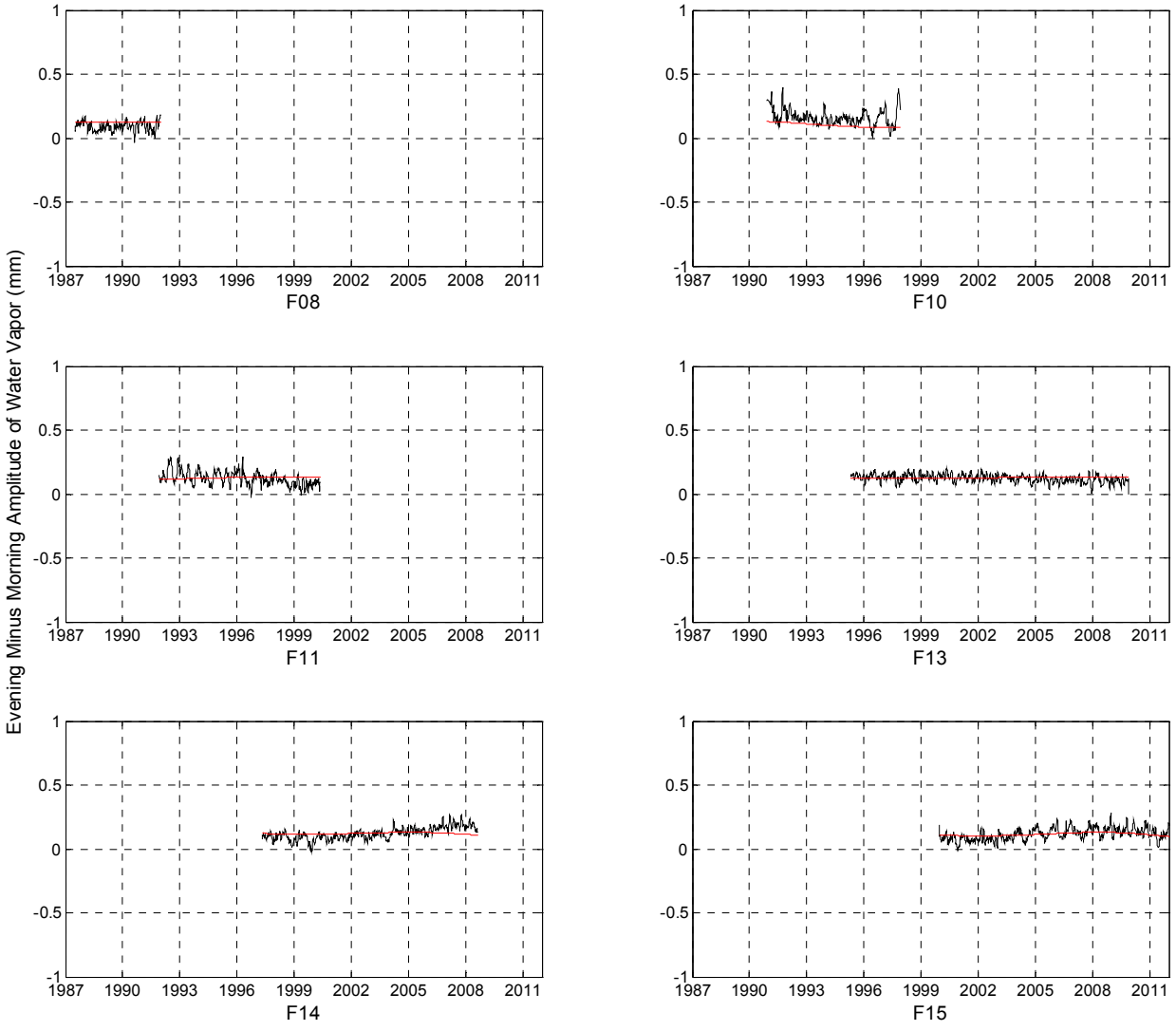

Figure 14. Evening minus morning amplitude of water vapor: $G_{vap}(t)$. The black curves are the observations, and the red curves are a simple diurnal model.

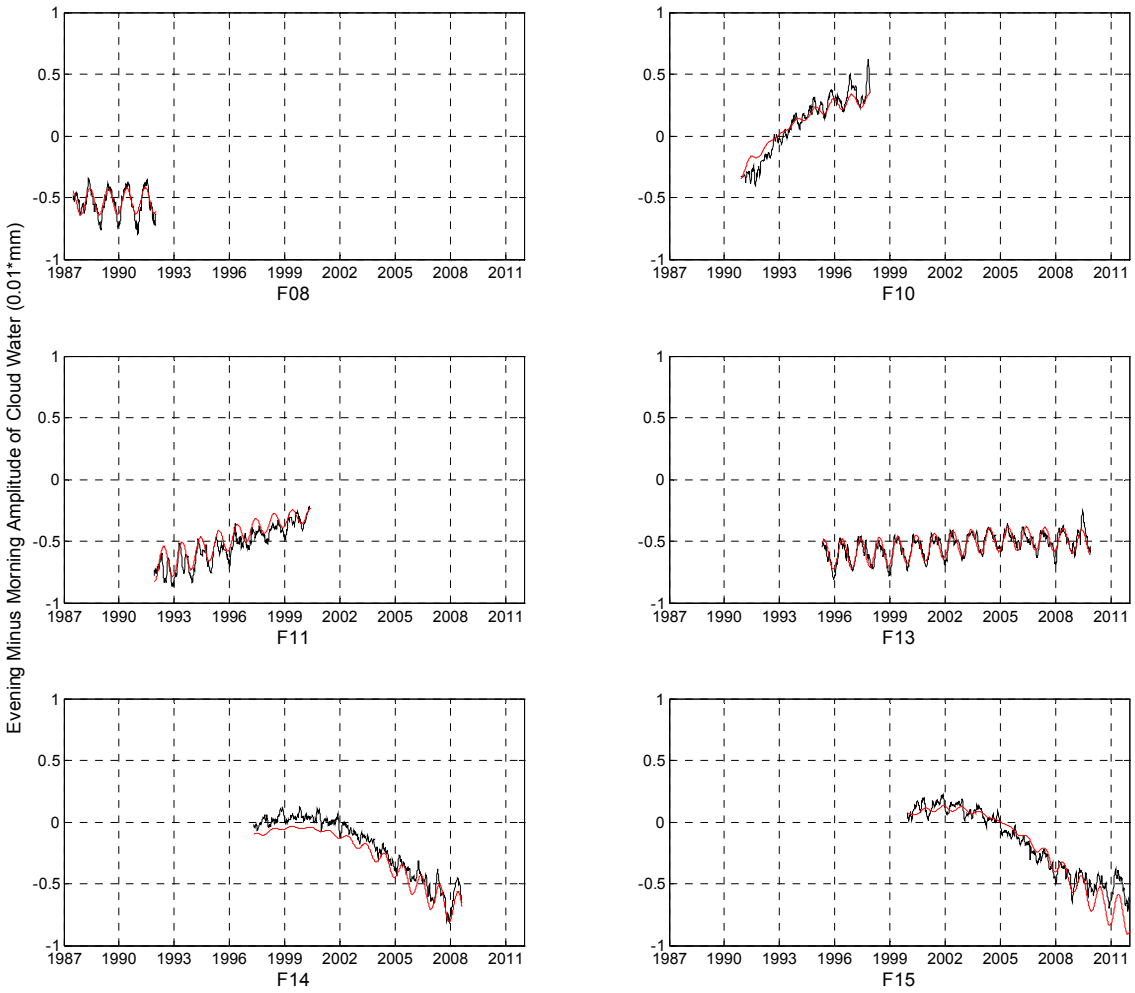

Figure 15. Evening minus morning amplitude of cloud water: $G_{cld}(t)$. The black curves are the observations, and the red curves are a simple diurnal model.

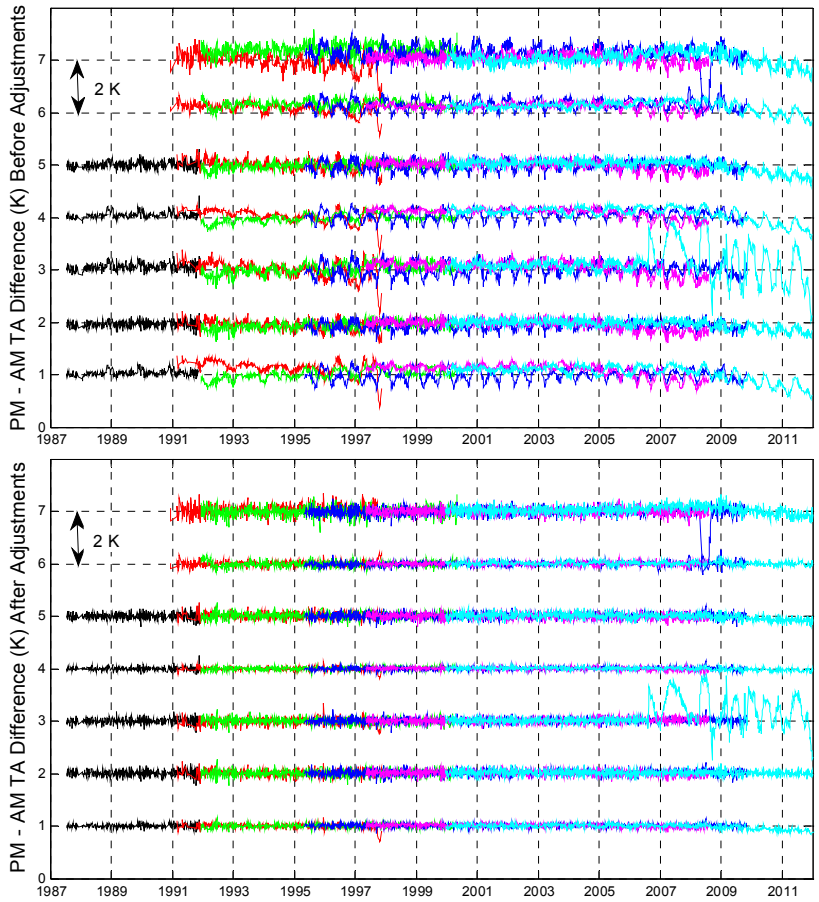

Figure 16. The pm minus am T_A difference for the 6 SSM/Is, with each SSM/I shown in a different color as indicated in Table 6. The top (bottom) frame shows the results before (after) applying adjustments. The labels on the vertical axis denote channel number (1=19V through 7=85H). The vertical scale for the T_A differences is such that 2 K corresponds to the distance between the channel zero lines. The 22V channel for the F15 SSM/I (cyan curve) shows residual errors due to the RADCAL beacon that turned on in August 2006. Also, the 85H channel for the F13 SSM/I (blue curve) shows an unexplained anomaly in 2008. Otherwise, the adjusted results show good pm versus am agreement.

2.4.13 Inter-Satellite Consistency Before and After Adjustments

To conclude our analysis, we show the T_A differences $\delta T'_A(i, j)$, as defined by (15), between pairs of SSM/Is flying on different satellites at the same time. Figure 17 shows $\delta T'_A(i, j)$ before and after applying the adjustments given by (17). The figure shows all 11 SSM/I overlapping pairs, with each overlap shown as a different color. The color coding is given in Table 2. Some colors can be reused for the later overlap cases because they are separated from the earlier cases. Each point in the $\delta T'_A(i, j)$ time series represents a global 5-day average. Before the adjustments are made, large inter-satellite differences of 1-2 K can be seen. After the adjustment, the root-mean-squared value of $\delta T'_A(i, j)$ averaged over all overlaps is about 0.1K except for 85H which is 0.2 K.

2.4.14 Version 7 Calibration as Compared to Version 6

Here we discuss the major differences between the Version 6 and Versions 7 calibration. The details on the V6 calibration can be found in *Wentz* [2010]. Table 10 highlights these differences, which we will now discuss.

The V6 calibration was done in 2006 and hence did not include the end of the F13, F14, and F15 missions. The local equator crossing time for F14 and F15 drifted considerably after 2006, and as a consequence the on-board thermal environment changed significantly as evidenced by the thermistor readings shown in the Appendix. The V7 calibration was completed at the begin of 2012 and includes complete mission observations from all SSM/Is except for F15 that continues to operate as of January 2013.

To establish an absolute reference for V6, the unadjusted T_As for all 6 SSM/Is up to mid-2006 were avearaged together. This average was then taken as the absolute reference, and additive T_A offsets were applied to each SSM/I to make them agree with this average value. The prelaunch measurements of the antenna spillover η and cross polarization coupling χ were then used to convert the V6 T_As to T_Bs. There were signficant differences (1-2 K) between V6 T_Bs and the RTM, and additional offsets needed to be applied to the V6 T_Bs before they could be used for geophsical retrievals. For V7, the absolute calibration is done by adjusting η and χ for a particular SSM/I so that its T_A measurements agree with the RTM in a global, mission-long sense as is dicussed in Section 3.4.4. The V7 T_Bs can be directly ingested by the retrieval algorithm with no futhere adjustments required. Since the RTM is being used as the absolute calibration reference, other MW imagers like WindSat, AMSR-E, and TMI can be calibrated similarly with out their calibration being tied to the SSM/I calibration.

Table 10. Major Differences between Version 6 and Version 7 Calibration

	Version 6	**Version 7**
Calibration Time Period	1987-2006	1987-2011
Absolute Calibration	Average of unadjusted T_A for all SSM/I	RTM is absolute reference
Absolute Inter-Satellite Biases	Removed by fixed T_A offsets	Removed by APC adjustments
Relative Inter-Satellite Biases	Removed by zonal T_A offsets	Hot target adjusted using $\Delta T_h(\alpha, \beta)$
PM versus AM T_A Differences	Lump into EIA adjustment	Hot target adjusted using $\Delta T_h(\psi, t)$
F08 SSM/I Closure Problem	Not realized	Corrected using $\Lambda_{F08}(t)$
Handling of F10 SSM/I	Zonal, seasonal, time varying T_A offsets	Non-linearity correction table $\Lambda_{F10}(\psi, t)$
Pointing Geometry	Adjustments made to EIA	No EIA adjustment required

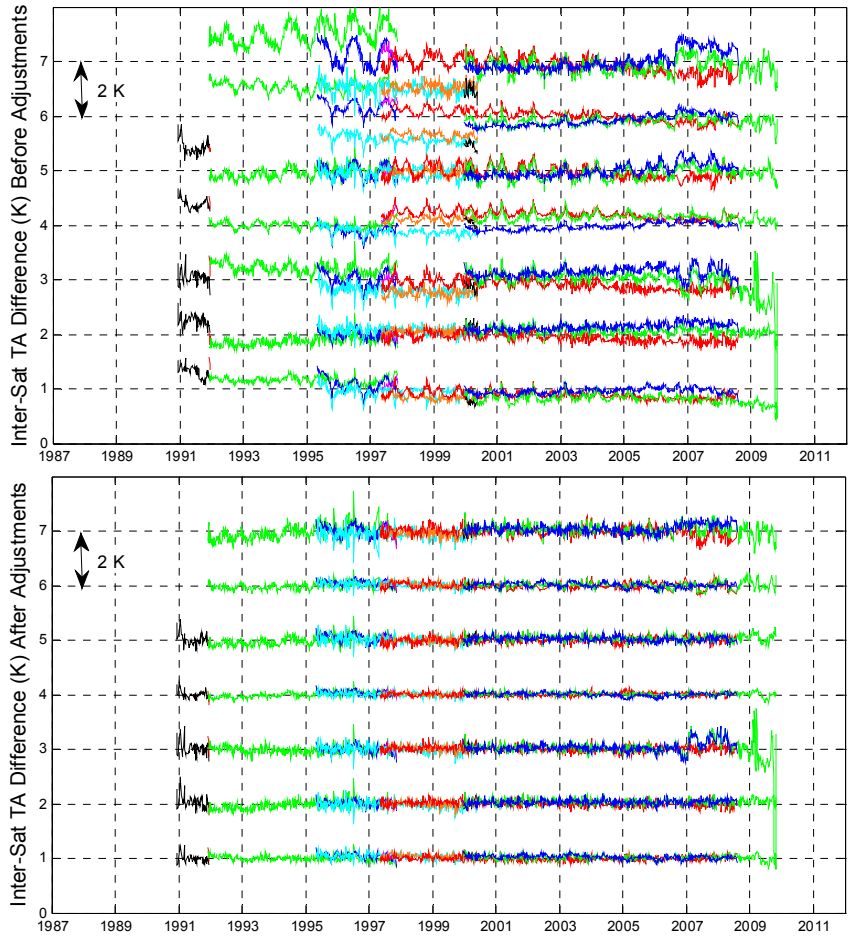

Figure 17. Inter-Satellite SSM/I T_A differences $\delta T'_A(i, j)$ for the 11 pairs of overlapping SSM/Is. Each overlap period is shown in a different color with the color coding given by Table 2. The top (bottom) frame shows the results before (after) applying adjustments. The labels on the vertical axis denote channel number (1=19V through 7=85H). The vertical scale for the T_A differences is such that 2 K corresponds to the distance between the channel zero lines. The 22V channel for the F15 SSM/I (2006-2009 blue and green curves) shows residual errors due to the RADCAL beacon that turned on in August 2006. Otherwise, the adjusted results show good agreement.

For V6, the inter-satellite biases, both absolute and relative, were removed by adding offsets to the T_A. These offsets were function of spacecraft orbit position ψ and time of year (i.e., seasonal adjustments). They were empirical with no physical basis. The V7 calibration is based on adjustments to the physical properties of the SSM/I calibration system, such as the antenna pattern characteristics, the effective temperature of the hot target, and non-linearity effects.

In doing the V6 calibration, the differences in the observed pm − am T_As were incorrectly interpreted as an error in specifying the EIA θ_i. The reason for this misinterpretation was that the F10 pm − am T_As showed a large 122-day 0.5 K harmonic that was associated with the same harmonic in θ_i. We mistakenly attributed this to an error in specifying θ_i. As it turned out, this problem was due to the EIA dependency in V6 RTM not being quite correct. Subsequent to the V6 development, the RTM was revised [*Meissner and Wentz*, 2012] based on WindSat and AMSR-E observations, which are at a variety of θ_i ranging from 50^o to 56^o. This variety of θ_i provided the means to refine and improve EIA dependency of the RTM. When the revised RTM used herein is applied to the F10 SSM/I, the 0.5 K harmonic in the F10 pm − am T_As reduces to less than 0.1 K (see Section 3.4.8), and an adjustment to θ_i is neither justified nor required. F10's 122-day θ_i harmonic provides us with an excellent verification of the V7 RTM. The improvement of the EIA dependency in V7 RTM was just based on WindSat and AMSR-E, and the F10 results were a pleasant surprise.

The F08 SSM/I closure problem was not realized during the V6 calibration. One of the strengths of the V7 calibration is the simultaneous consideration of T_A calibration and the resulting geophysical retrievals. The closure analysis is a direct extension of this methodology and is providing us with a valuable new calibration tool.

The handling of the F10 SSM/I calibration has always been a problem. When doing the V7 calibration, we realized the internal temperature of the F10 receivers had been anomalously high throughout its mission. Possibly that explains the unique calibration problems experienced by F10. As mentioned above, for V6 we mistakenly attributed some of the F10 calibrations problems to misspecifying θ_i, and the remaining problems were fixed by adding T_A offsets that were a function of spacecraft orbit position ψ and time of year. T_A drift corrections were also applied to all of the channels for V6. The V7 calibration For F10 is a significantly cleaner. No unique (i.e., any different than the other 5 SSM/Is) adjustments are applied to the 19H and 37H channels except the very small (0.05 K) correction given by equation (41). For the other F10 channels, we assume the high temperature of the receivers is causing a non-linear response, and the $\Lambda_{F10}(\psi, t)$ correction is applied.

2.5 Algorithm Output

The algorithm output is RSS L1B brightness temperature data. One file is written for each SSM/I orbit. This data is then converted to netcdf4 using a IDL 8.2 routine. An example netcdf file name is:

RSS_SSMI_FCDR_V07R00_F10_D19910201_S1322_E1422_R00886.nc,

Where:

V07R00 corresponds to the version number

F10 is the satellite

19910201 is the year, month, and day of the start time

S1322 is the stat time in hhmm format

E1422 is the end time in hhmm format

R00886 refers to the obit number.

These files are then assembled into monthly tar files for transmission to NCDC.

An example monthly file name is:

RSS_SSMI_FCDR_V07R00_F10_D199103.tar

Where:

V07R00 corresponds to the version number

F10 is the satellite

D199103 refers to the year and month of the data.

3. Practical Considerations

3.1 Quality Assessment and Diagnostics

The use of quality flags variables in each netCDF file allows for detailed footprint-level identification of radiance anomalies.

3.2 Algorithm Validation

The primary validation of the V7 TA and TB datasets is through their resulting geophysical retrievals. For example, one of the most critical requirements for an CDR dataset is that it be free of spurious long-term trends. Validation of this requirement can be obtained by analyses of the resulting geophysical retrievals. Comparison of the wind speeds retrieved from the V6 TB with buoys and scatterometers indicates a trend error of 0.05 m/s/decade at the 95% confidence level over the 1987 to 2006 time period [Wentz et al., 2007]. The standard error on the water vapor trend (1987-2006) is 0.2%

per decade [Wentz and Schabel, 2000]. With respect to precipitation, when diurnal effects are removed, the agreement among different SSM/I is 3% [Hilburn and Wentz, 2008b]. Note that some of this 3% difference is probably due to residual geophysical effects such as 'beamfilling' rather than TB intercalibration error. Still, 3% is the best inter-sensor precipitation agreement yet achieved from any SSM/I TB dataset.

4. References

Christy, J. R., R. W. Spencer, et al. (2000), MSU Tropospheric Temperatures: Dataset Construction and Radiosonde Comparisons, *Journal of Atmospheric and Oceanic Technology, 17*(9): 1153-1170.

Colton, M. C. and G. A. Poe (1999), Intersensor Calibration of DMSP SSM/I's: F-8 to F-14, 1987-1997, *IEEE Trans. Geoscience and Remote Sensing, 37*, 418-439.

Hilburn, K. A. and F. J. Wentz (2008), Mitigating the Impact of RADCAL Beacon Contamination on F15 SSM/I Ocean Retrievals. *Geophysical Research Letters, 35.* L18806, doi:10.1029/2008GL034914.

Hilburn, K. A. (2009), Including Temperature Effects in the F15 RADCAL Correction. *RSS Technical Report 051209*, , Remote Sensing Systems, Santa Rosa, CA, http://www.remss.com/papers/RSS_TR051209_RADCAL.pdf

Hollinger,J., R. Lo, G. Poe, R. Savage, and J. Pierce (1987), Special Sensor Mirowave/Imager User's Guide, *Naval Research Laboratory Report*, Washington DC.

Mears, C. A., M. C. Schabel, and F. J. Wentz (2003), A Reanalysis of the MSU Channel 2 Tropospheric Temperature Record. *Journal of Climate, 16*, 3650-3664.

Meissner, T. and F. Wentz (2002), An updated analysis of the ocean surface wind direction signal in passive microwave brightness temperatures *IEEE Trans. Geoscience and Remote Sensing, 40*(6), 1230.

Meissner, T. and F. Wentz (2003), A radiative transfer model function for 85.5 GHz SSM/I ocean brightness temperatures, *Radio Science, 38*(4), 8066.

Meissner, T. and F. Wentz (2004), *The complex dielectric constant of pure and sea water from microwave satellite observations*, *IEEE Trans. Geoscience and Remote Sensing*, *42*(9), 1836.

Meissner. T., and F. Wentz (2012), *The emissivity of the ocean surface between 6 - 90 GHz over a large range of wind speeds and Earth incidence angles*, *IEEE Trans. Geoscience and Remote Sensing, 50*(8), 3004.

Smith, D. K., C. A. Mears, and F. J. Wentz (2002), Detection and characterization of diurnal winds using QuikScat data, *2002 International Geoscience and Remote Sensing Symposium*, IGARSS, IEEE, Toronto, Canada, 735-737.

Sun, N. and Fuzhong Weng (2008), Evaluation of Special Sensor Microwave Imager/Sounder (SSMIS) Environmental Data Records, *IEEE Trans. Geoscience and Remote Sensing, 46*(4) 1006-1016

Twarog, E. M., W. E. Purdy, P. W. Gaiser, K. H. Cheung, and B. E. Kelm (2006), WindSat On-Orbit Warm Load Calibration, *IEEE Trans. Geoscience and Remote Sensing 44*(3) 516-529.

Wentz, F. J. (1983), A model function for ocean microwave brightness temperatures, *J. Geophy. Res. 88,* 1892-1908.

Wentz, F. J. (1988), User's Manual SSM/I Antenna Temperature Tapes. *RSS Technical Report 032588*, Remote Sensing Systems, Santa Rosa, CA.

Wentz, F. J., (1991), Revision 1 User's Manual SSM/I Antenna Temperature Tapes. *RSS Technical Report 120191*, Remote Sensing Systems, Santa Rosa, CA. http://www.remss.com/papers/ssmi/TA/SSMI_TA_manual_rev_1_part_1.pdf, http://www.remss.com/papers/ssmi/TA/SSMI_TA_manual_rev_1_part_2.pdf

Wentz, F. J., (1993), Revision 2 User's Manual SSM/I Antenna Temperature Tapes. *RSS Technical Report 120193*, Remote Sensing Systems, Santa Rosa, CA. http://www.remss.com/papers/ssmi/TA/SSMI_TA_manual_rev_2.pdf

Wentz, F. J., (1997), A Well Calibrated Ocean Algorithm for Special Sensor Microwave/Imager*, J. of Geophysical Research, 102*, 8703-8718.

Wentz, F. and T. Meissner (2000), AMSR Ocean Algorithm (Version 2) Algorithm Theoretical Basis Document (ATBD), *RSS Technical Report 121599A-1*, Remote Sensing Systems, Santa Rosa, CA, http://www.remss.com/papers/amsr/AMSR_Ocean_Algorithm_Version_2.pdf.

Wentz, F. J. (2010), The Version-6 Calibration of SSM/I, *RSS Technical Report 102210*, Remote Sensing Systems, Santa Rosa, CA. http://www.remss.com/papers/tech_reports/Wentz_SSMI_Version6_Calibration.pdf